Impact of Conical Hypersonic Boundary Layer Transition on Skin Drag and Heating

Carleton P. Knisely,* Christopher Haley,† and Xiaolin Zhong‡
University of California, Los Angeles, California, 90095, USA

It is commonly known that transition location has a significant effect on drag and heating in hypersonic boundary layers, but the effect is not typically systematically quantified. This study provides an estimate of skin drag force and aerodynamic surface heating rate in laminar and turbulent hypersonic conical flow. The skin friction coefficient (c_f) and Stanton number (St) for seven hypersonic flow cases (Mach 4.96 to Mach 10) over axisymmetric cones were computed using Direct Numerical Simulation (DNS) assuming both perfect and thermochemical nonequilibrium gas models. Laminar and turbulent correlations for c_f and St using flow properties obtained from the DNS and an axisymmetric shock (Taylor-Maccoll) analysis were compared to DNS, in which reasonable agreement was found. Laminar flow has up to 70% lower drag and heating than the fully turbulent case. Alternatively, turbulent flow has up to 230% higher drag and 240% higher heating compared to laminar flow. The wall temperature has only a small impact on skin drag, however it can have a more significant effect on surface heating. Overall, results show similar significant relative reductions in skin drag and heating, with higher enthalpy flows exhibiting the largest absolute reductions.

Nomenclature

c_p	=	Specific heat at constant pressure [J/kg-K]	c_f	=	Skin friction coefficient [-]
F_{skin}	=	Skin drag force [N]	h	=	Enthalpy [MJ/kg]
κ	=	Thermal conductivity [W/m-K]	M	=	Mach number [-]
p	=	Pressure [kPa]	Pr	=	Prandtl number [-]
$\dot{q}$	=	Heat transfer rate [kW/m^2]	$\dot{Q}$	=	Surface heating rate [kW]
r	=	Recovery factor [-]	r_n	=	Nose radius [m]
R_f	=	Reynolds analogy factor [-]	Re_x	=	Compressible Reynolds number [-]
s	=	Streamwise distance [m]	s_{tr}	=	Transition location [m]
St	=	Stanton number [-]	T	=	Translation-rotation temperature [K]
T_V	=	Vibration temperature [K]	u	=	Wall-tangent velocity [m/s]
μ	=	Dynamic viscosity [kg/m-s]	ρ	=	Density [kg/m^3]
τ_w	=	Wall shear stress [Pa]			

Subscripts

aw	=	Adiabatic wall	e	=	Boundary layer edge
w	=	Wall	0	=	Stagnation
∞	=	Free stream			

*Graduate Student, Mechanical and Aerospace Engineering, carleton.knisely@gmail.com, AIAA Student Member.
†Graduate Student, Mechanical and Aerospace Engineering, clhaley@g.ucla.edu, AIAA Student Member.
‡Professor, Mechanical and Aerospace Engineering, xiaolin@seas.ucla.edu, AIAA Associate Fellow.

I. Introduction

To study hypersonic flow is to study the hypersonic heating problem—that in such high-speed flows drag work ultimately shows up as heat conducted to the vehicle or convected to its wake.[1] The reason for this is the role skin friction drag plays in aerodynamic heating. Skin friction is so consequential that the study of hypersonic boundary layer transition has been an area of active research since the 1960's.[2] Hypersonic boundary layer transition research is typically highly detailed work, concerned with boundary layer stability, receptivity, and transition studies.[3,4] The labor and knowledge needed to obtain these results is time consuming and quite frankly difficult to access beyond academia. Currently, there is a gap between research and practical application, motivating the need to easily and accurately quantify the drag and heating on a hypersonic vehicle with simple geometry.[5] Empirical correlations derived by van Driest[6] and corrected for compressibility by Goyne[7] are easily computed but they are highly dependent on boundary layer edge conditions, which may be difficult to obtain accurately. By contrast Direct Numerical Simulation (DNS) can provide an accurate computation of skin drag and surface heating but requires high performance computing (HPC) resources and time investment. This work aims to create an accurate but easily computable method for determining skin drag and surface heating on simple geometries using the compressible correlations transformed for conical flow and utilizing laminar DNS results (which lack turbulence modeling) and the Taylor-Maccoll solutions of a compressible conical flow.

The modified correlations provide a simple tool for estimating the effect of skin friction on surface heating beyond its first-order relationship by providing an easy to use but improved means to analyze laminar and turbulent skin friction. To discuss this improvement further we must first introduce the first order relationship of skin friction on surface heating. A simple construct of the hypersonic heating problem considers the atmospheric deceleration of a hypersonic object. The drag work done on the object acts to increase the temperature of the object and the temperature of the air in its wake. A tractable equation is obtained by applying Newton's second law to the decelerating object and applying a heat-transfer rate based on the objects velocity and enthalpy potential between the hot gas and cool body. After making the appropriate substitutions, simplifications and approximations, which are omitted for brevity but can be found in,[1] the following equation is obtained

$$Q_f = \frac{1}{2}\frac{C_f}{C_D}\frac{1}{2}\frac{W}{g}V_i^2 \tag{1}$$

where Q_f is the heat transfered to the object, C_f is skin friction coefficient, C_D is the total drag, W is the object's weight, g is gravitational acceleration and V_i is the object's initial velocity. It is apparent that Q_f is reduced when $\frac{C_f}{C_D}$ is minimized. This is evident in the design of the space shuttle which seeks to maximize C_D. It is also apparent to see that Q_f is reduced when W is minimized, however this is an aim better suited to a structural engineer and material scientist than a fluid mechanist. A keen eye will note that Q_f is also reduced when C_f is minimized. The simplest approach to minimizing C_f is to promote laminar flow over turbulent flow. The modified correlations described in this paper provide an easy means to produce quantifiable estimations of fully laminar or fully turbulent skin friction coefficients from CFD simulations or analytical conical flow solutions. This simple tool can also be used to estimate the benefit of delaying transition.

Research on practical ways to delay transition is an area of some inquiry within the hypersonic boundary layer stability community. Considerable progress has been made with novel ideas such as surface blowing,[8] porous coatings,[9] and transition-delay surface roughness.[10–12] In fact the first time these modified correlations were used in a boundary layer stability context was in trying to quantify the benefit of employing transition-delay roughness.[13] This paper proposes that these modified correlations can be used to as a design tool to quantify the benefit of delaying transition. This can help to decide whether employing novel transition-delaying strategies is a worthwhile investment. Our results show that even a small delay in transition can result in an appreciable reduction in skin friction and thus in surface heating.

This paper also considers some of the limitations of the correlations as they are empirically derived. When applied to high enthalpy thermochemical nonequilibirum simulations the correlation results, as will be seen later, are less than exceptional. This limits the utility of the correlations to perfect gas CFD simulations and analytical solutions, but also advocates for the derivation of empirical correlations incorporating high enthalpy real gas effects. Furthermore, the results also advocate that high-enthalpy flow is by itself worth investigating.

Another utility of these correlations explored in this work is a light-weight means to check for agreement between correlations and simulation. A simulation can subsequently by verified (a sanity check) within the confines of the empirical limits of the correlation and the simulation results to which the correlations pertain. This can be a convenient option for verification when a full scale experimental validation is infeasible or unavailable.

Lastly we suggest these modified correlations can be extended to more complex geometries. These correlations were originally obtained from low-speed (incompressible) experiments on a flat plate.[6] They were first modified by Goyne, who applied a compressibility correction so they could be applied to a high-speed flow up to 9 MJ/kg stagnation enthalpy over a flat plate.[7] These correlations were further transformed in this work so they could be applied to conical flow fields. This shows how an otherwise unassuming correlation can be extended beyond its original intentions.

II. Methods

A. Overview of Strategy

This work aims to quantify the impact of transition location on skin drag and aerodynamic surface heating for hypersonic flow conditions using high-order accuracy numerical tools and empirical correlations. The general strategy is to compute the skin friction coefficient from CFD simulations via

$$c_f = \frac{\tau_w}{\frac{1}{2}\rho_e u_e^2} \tag{2}$$

where $\tau_w = \mu \frac{du}{dy}\Big|_{y=0}$ and μ is the dynamic viscosity of the fluid at the wall, $\frac{du}{dy}$ is the wall-normal velocity gradient at the wall ρ_e and u_e are the density and wall-tangent velocity at the boundary layer edge, respectively. Additionally, the Stanton number, the ratio of heat transfered into a fluid to its thermal capacity,

$$St = \frac{\dot{q}}{\rho_e u_e \left(h_{aw} - h_w\right)} \tag{3}$$

is computed, where $\dot{q} = \kappa \frac{dT}{dy}\Big|_{y=0}$ with κ being the fluid thermal conductivity at the wall and $\frac{dT}{dy}$ being the wall-normal temperature gradient at the wall, and h_{aw} and h_w are the adiabatic wall enthalpy and the isothermal wall enthalpy, respectively. The skin friction coefficient and Stanton number from the simulation are then compared to empirical correlations based on perfect gas flow for the same parameters. The empirical correlations rely on flow variables at the boundary layer edge, which can either be taken directly from the DNS or from the Taylor-Maccoll analysis for axisymmetric shocks in perfect gas flow. A schematic of this procedure is summarized in Fig. 1. The accuracy of the correlations is assessed by comparing to both the perfect gas and nonequilibrium simulations. Once good agreement between the simulations and correlations is obtained, the correlation for skin friction coefficient and Stanton number are integrated over the surface of the cone to obtain the overall drag force and surface heating rate. The transition location is defined as the point at which the integral is computed with the turbulent correlation instead of the laminar correlation. This strategy allows for a direct analysis of the impact of transition location on skin drag and aerodynamic surface heating, and allows for qualitative assessment of the correlations to model flow with real gas effects.

B. Steady Flow Field Solution Overview

The high-order shock-fitting DNS code developed by Haley and Zhong[12] assumes a perfect gas model and is used to compute the steady mean flow for Cases A, B and C. The code utilizes a 5th order upwind scheme in space and a 1st order Runge-Kutta scheme in time. Details of the perfect gas code can be found in Haley and Zhong.[12]

A thermochemical nonequilibrium DNS code developed and verified by Mortensen and Zhong[14–19] and recently used by Knisely and Zhong[20,21] is used to compute the steady base flow in Cases 1 through 4. The code also utilizes a high-order shock-fitting method extended from a perfect gas flow version by Zhong[22] to compute the flow field between the shock and the body. The rotational mode is assumed to be fully excited with a five-species non-ionizing model used to simulate air (N_2, O_2, NO, N, and O) with finite-rate chemistry. Two-temperatures are used to represent translation-rotation energy and vibration energy.

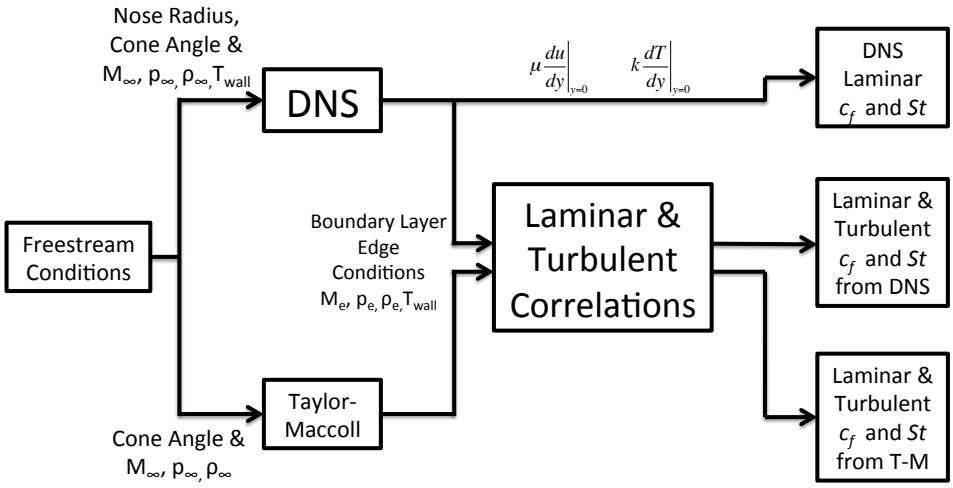

Figure 1. Schematic of methods for computing c_f and St for comparison and analysis.

Although the governing equations are more complex than the perfect gas version, similar numerical methods are used to solve for the flow field. Namely, the same shock fitting technique and 5th order upwind scheme are largely the same. Lastly, the solution is also advanced in time using a 1st order Runge-Kutta scheme. The full details of the numerical method and approach can be found in Mortensen's dissertation[19] and in recent works by Knisely and Zhong.[20,21]

The skin friction coefficient from the steady flow field simulation is calculated via Eq. 2 and the Stanton number is computed via Eq. 3. The boundary layer edge conditions are defined as the wall-normal location at which $u(y) = 0.99u_{edge}$, where u_{edge} is the wall-tangent velocity immediately downstream of the shock. All parameters can be directly obtained from the flow field solution with the exception of h_{aw}. The adiabatic wall enthalpy is computed via

$$h_{aw} = h_e + r\left(h_0 - h_e\right) \tag{4}$$

where h_e is the flow enthalpy at the boundary layer edge, h_0 is the edge stagnation enthalpy, and r is the recovery factor given by

$$r = \begin{cases} Pr^{1/2} & \text{for laminar flow,} \\ Pr^{1/3} & \text{for turbulent flow} \end{cases} \tag{5}$$

where Pr is the Prandtl number

$$Pr = \frac{c_p \mu_e}{k} \tag{6}$$

which is assumed to have a constant value of $Pr = 0.72$.

C. Taylor-Maccoll Axisymmetric Shock Solution

The boundary layer edge conditions may also be obtained by performing the Taylor-Maccoll[23] analysis for axsymmetric inviscid compressible conical flow. Transforming the governing equations to polar coordinates and assuming the flow variables do not vary in the azimuthal and radial directions results in a second order ordinary differential equation for $V_r(\theta)$ between the shock and the body:

$$\frac{\gamma - 1}{2}\left[1 - V_r^2 - \left(\frac{dV_r}{d\theta}\right)^2\right]\left[2V_r + \cot\theta \frac{dV_r}{d\theta} + \frac{d^2V_r}{d\theta^2}\right] - \frac{dV_r}{d\theta}\left[V_r \frac{dV_r}{d\theta} + \frac{dV_r}{d\theta}\frac{d^2V_r}{d\theta^2}\right] = 0 \tag{7}$$

where $\gamma = c_p/c_v = 1.4$, V_r is the radial component of velocity, $V_\theta = dV_r/d\theta$ is the angular component of velocity, and θ is the polar angle. The velocity is normalized by the maximum theoretical velocity, $V_{max} = \sqrt{2c_pT_0}$. Additionally, it can be shown that the nondimensional velocity and Mach number are

related by

$$V^2 = V_r^2 + V_\theta^2 = \frac{1}{1 + \frac{2}{(\gamma-1)M^2}}. \tag{8}$$

To solve for the conditions at the boundary layer edge an initial guess for the axisymmetric shock angle is required, for which the 2D oblique shock relations are used. Flow conditions immediately downstream of the shock are also computed. With the initial shock angle and downstream flow conditions assumed, Eq. 7 is integrated using an adaptive time-step variable-order Runge-Kutta method for stiff ODEs (`ode15s` in MATLAB[24]) from the shock angle β towards the surface of the cone. When $V_\theta = dV_r/d\theta = 0$ within a tolerance of $\pm 1E-05$ the integration is stopped, indicating the surface of the cone assuming a no-flow-through condition. If the angle θ at the end of integration matches the prescribed cone half-angle within a tolerance of $\pm 1E-10$, the solution is found. If not, the guess for β is updated using the bisection method and the integration is repeated until θ at the end of integration matches the prescribed cone half-angle within the tolerance. The Mach number at the end of integration is then computed using Eq. 8. This Mach number represents the boundary layer edge Mach number. Isentropic relations between Mach numbers immediately downstream of the shock and at the boundary layer edge are used to compute pressure, temperature, density, etc. at the boundary layer edge. The Taylor-Maccoll analysis outlined here has been successfully verified against Bartlett,[25] shown in Fig. 2. It should be noted that the symbols in Fig. 2 have been digitized by hand, which may have introduced some error. Additionally, the Taylor-Maccoll analysis agrees with Chart 7 of NACA Report 1135.[26] For a free stream Mach number of 5, the computed boundary layer edge Mach number is 4.7148, while the chart indicates a boundary layer edge Mach number of 4.71. For a free stream Mach number of 10, the code and chart are also in agreement. The code predicts a boundary layer edge Mach number of 8.7725, whereas the chart predicts 8.77.

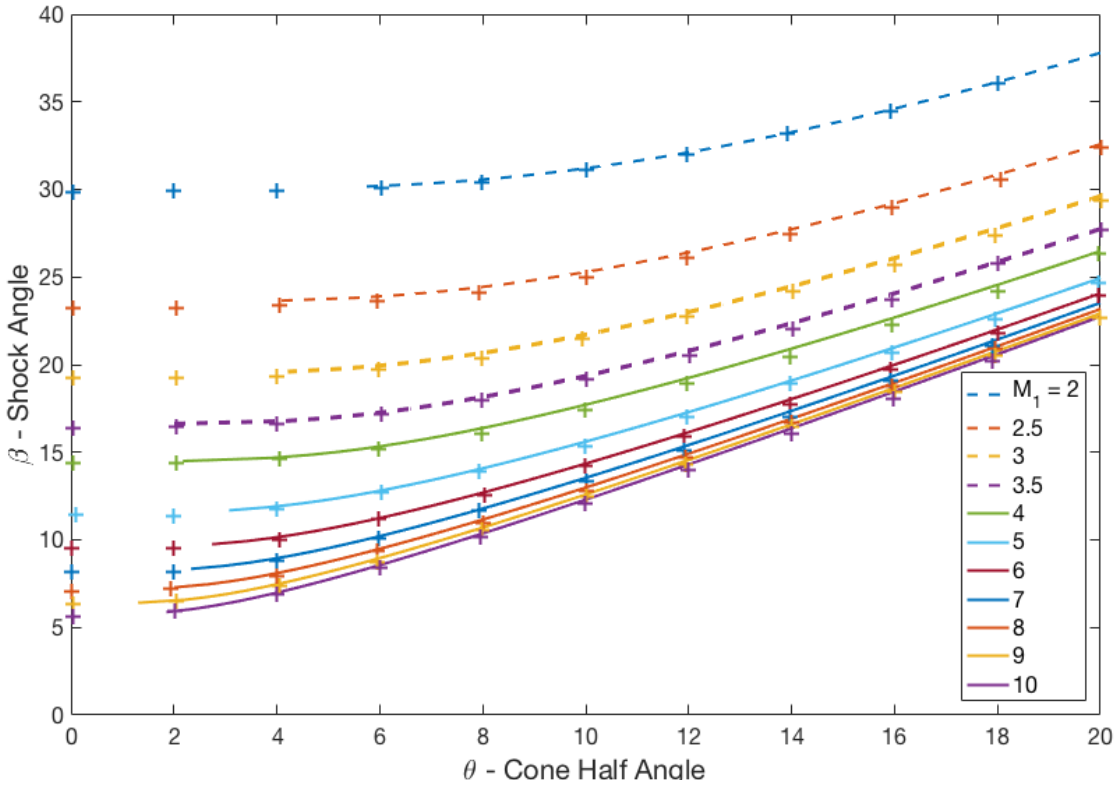

Figure 2. Comparison of shock angle as a function of axisymmetric cone angle. Lines: Taylor-Maccoll solution. Symbols: Bartlett's[25] Fig. 2.

D. Skin Friction Coefficient and Stanton Number Correlations for a Flat Plate

The compressible skin friction coefficient and Stanton number correlations were obtained from the incompressible flat plate correlations by Van Driest[6] and Eckert[27] using methodology set forth by Goyne *et al.*[7] The flat plate correlations were extended to a sharp cone via the method outlined by Crabtree *et al.*[28] The edge conditions are either the local boundary layer edge conditions extracted from DNS or the boundary layer edge conditions computed by the Taylor-Maccoll analysis.

First, the steps to compute the skin friction coefficient, c_f, are presented. The underlying correlations for incompressible flow are

$$c_{f,i} = \begin{cases} 0.664 Re_{x,i}^{-0.5} & \text{for laminar flow,} \\ 0.0592 Re_{x,i}^{-0.2} & \text{for turbulent flow} \end{cases} \tag{9}$$

where the subscript i indicates incompressible flow and $Re_{x,i}$ is the incompressible Reynolds number. To transform the incompressible skin friction coefficient, $c_{f,i}$ to the compressible skin friction coefficient, c_f, the procedure of Goyne *et al.*[7] is followed. The compressibility transformation can be written in terms of the functions F_c and F_{Re_x}:

$$c_{f,i} = F_c c_f \tag{10}$$

$$Re_{x,i} = F_{Re_x} Re_x \tag{11}$$

where

$$Re_x = \frac{\rho_e u_e x}{\mu_e} \tag{12}$$

is the compressible Reynolds number. To compute the functions F_c and F_{Re_x}, Eckert's[27] reference temperature, T^*, is used.

$$F_c = \frac{T^*}{T_e} \tag{13}$$

$$F_{Re_x} = \frac{\mu_e T_e}{\mu^* T^*} \tag{14}$$

where

$$T^* = 0.5 T_w + 0.22 T_{aw} + 0.28 T_e \tag{15}$$

with T_{aw} computed from Eq. 4. The dynamic viscosity μ^* can be computed via Sutherland's law:

$$\mu(T) = \mu_r \left(\frac{T}{T_0} \right)^{3/2} \frac{T_0 + T_s}{T + T_s} \tag{16}$$

where for air $\mu_r = 1.7894 \times 10^{-5}$ Ns/m^2, $T_0 = 288$ K, and $T_s = 110.33$ K.

To compute the skin friction coefficient correlation, the compressible Reynolds number, Re_x, is first computed using given boundary layer edge conditions via Eq. 12. The compressible Reynolds number, Re_x, is transformed to the incompressible Reynolds number, $Re_{x,i}$ via Eq. 11 for both laminar and turbulent correlations. This involves computing the compressibility transformation function F_{Re_x} for both laminar and turbulent conditions. Then, the incompressible skin friction coefficient, $c_{f,i}$, is computed for both laminar and turbulent flow using Eq. 9. Lastly, the incompressible skin friction coefficient, $c_{f,i}$, is transformed to the compressible skin friction coefficient, c_f, via Eq. 10 for both laminar and turbulent flow.

Computing the Stanton number correlation from the skin friction coefficient is quite straightforward. The Stanton number, St, and skin friction coefficient, c_f, are related via the Reynolds analogy factor, R_f, through

$$\frac{2St}{c_f} = R_f \tag{17}$$

where the Reynolds analogy factor is given by

$$R_f = \begin{cases} Pr^{-2/3} & \text{for laminar flow,} \\ 1.22 & \text{for turbulent flow} \end{cases} \tag{18}$$

E. Transformation of Correlations to Conical Geometry

Thus far, the correlations for c_f and St are only valid for a flat plate geometry. To transform these correlations to a conical geometry, the relatively simple procedure outlined by Crabtree *et al.*[28] is followed. Applying the Mangler transform to the boundary layer equations for a sharp cone shows that the local Stanton number is $\sqrt{3}$ times larger than that for a flat plate in laminar flow, at the same local Mach number. Alternatively, the local Stanton number for laminar flow on a cone may be obtained directly as being equal to the local Stanton number on a flat plate at Reynolds numbers of 1/3 times the cone Reynolds number, other local conditions being identical. These results also apply to skin friction coefficients.

For turbulent flow, for a cone in axial flow the local Stanton number is 1.15 times as great as for a flat plate under the same local conditions.[28] Alternatively, the local Stanton number for turbulent flow on a cone may be obtained directly as being equal to the local Stanton number on a flat plate at Reynolds number of 0.5 times the cone Reynolds number, other local conditions being identical. These factors also apply to the calculation of skin friction coefficients.

F. Calculation of Total Skin Drag and Heat Transfer Rate

Once good agreement between the simulation skin friction coefficient, c_f, and Stanton number, St, to the correlations is verified, the total skin drag and total surface heating rate can be computed depending on a specified transition location, s_{tr}. The overall idea is that because the simulation agrees well with the laminar correlation, the turbulent correlation can be used accurately as well. Therefore, if a pre-set transition location is considered, the laminar correlation is used upstream of this location, and the turbulent correlation is used downstream of this location.

The total skin drag force, F_{skin}, on the cone can be computed from the local skin friction coefficient correlation, c_f, via

$$F_{skin} = \int_{surf} c_f \frac{1}{2} \rho_e u_e^2 dA. \tag{19}$$

Similarly, the total heat transfer rate, $\dot{Q}$, can be determined from the local heat transfer rate, $\dot{q}$, using the Stanton number:

$$\dot{q} = St \rho_e u_e \left(h_{aw} - h_w\right) \tag{20}$$

$$\dot{Q} = \int_{surf} \dot{q} dA. \tag{21}$$

Thus, the total skin drag force, F_{skin}, and total heat transfer rate, $\dot{Q}$, to the cone can be determined based on the laminar and turbulent correlations for c_f and St and the transition location, s_{tr}. The computation of F_{skin} and $\dot{Q}$ as a function of s_{tr} can be summarized as:

$$F_{skin} = \int_{surf} \begin{cases} c_{f,laminar} \frac{1}{2} \rho_e u_e^2 dA & \text{if } s < s_{tr}, \\ c_{f,turbulent} \frac{1}{2} \rho_e u_e^2 dA & \text{if } s \geq s_{tr} \end{cases} \tag{22}$$

$$\dot{Q} = \int_{surf} \begin{cases} St_{laminar} \rho_e u_e \left(h_{aw} - h_w\right) dA & \text{if } s < s_{tr}, \\ St_{turbulent} \rho_e u_e \left(h_{aw} - h_w\right) dA & \text{if } s \geq s_{tr} \end{cases} \tag{23}$$

III. Flow Conditions

The steady flow field is obtained from DNS with two separate geometries. Case A, B, and C assume a perfect gas model and are a 0.5 meter long cone with a 7 degree half-angle. Cases A and C have a nose radii of 0.5 mm and Case B's nose radius is 0.05 mm. Cases 1 through 4 assume thermochemical nonequilibrium and are a 1 mm nose-radius, 1 meter long cone with a 5 degree half-angle. The free stream mass fractions are $c_{N_2} = 0.78$ and $c_{O_2} = 0.22$. In all cases the wall is assumed to be isothermal, and all free stream conditions reported are upstream of the bow shock. The flow conditions for the three cases are summarized in Table 1. Cases A and C share the same nose radius but have different free stream Mach numbers while Cases B and C share a similar freestream Mach number but different nose radii. Case 1 and Case 2 have the same free stream conditions, but the wall temperature is varied. Cases 3 and 4 are higher enthalpy cases than Cases 1

and 2. Case 4 is a cold-wall flow, whereas Case 3 is a hot-wall flow. Cases A, B and C have significantly lower free stream enthalpy; therefore the internal energy modes are not excited and the perfect gas assumption is valid. Additionally, Cases A, B and C have sharper nose radii and larger half-angle than Cases 1 through 4.

Table 1. Flow conditions for DNS simulations.

Case:	A	B	C	1	2	3	4	Units
M_∞	4.96	7.84	8	5	5	10	10	–
$H_{0,\infty}$	0.486	0.714	0.644	9.17	9.17	14.78	14.78	MJ/kg
ρ_∞	5.58E-2	2.2446E-2	2.4803E-2	2.322E-2	2.322E-2	1.91E-2	1.91E-2	kg/m^3
p_∞	1.3	0.344	0.331	10	10	4	4	kPa
Gas Model	Perfect	Perfect	Perfect	Noneq.	Noneq.	Noneq.	Noneq.	–
r_n	0.5	0.05	0.5	1	1	1	1	mm
T_w	297	297	297	300	1000	1000	300	K

A schematic of the flow field is shown in Fig. 3. The flow travels from left to right, with the outer edge of the computational boundary representing the bow shock. The surface of the cone is the lower boundary of the computational zone and is treated with an isothermal wall condition.

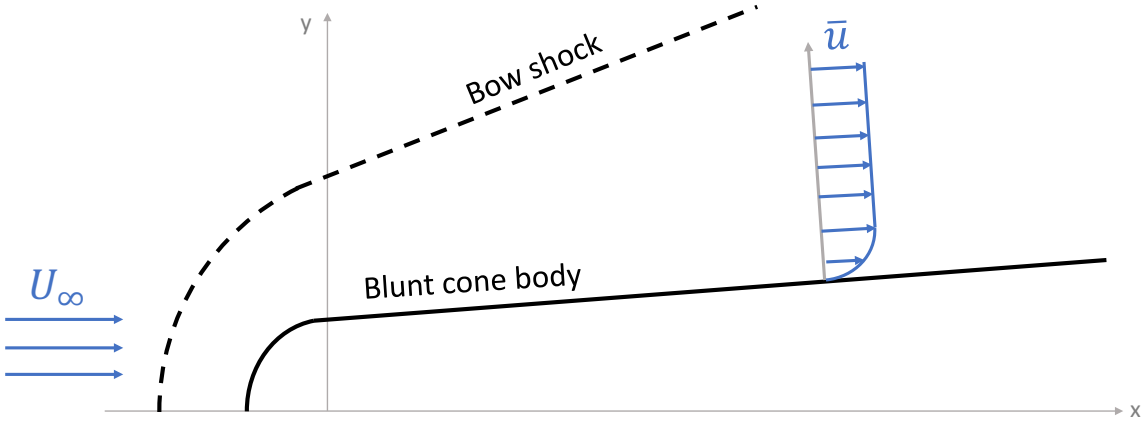

Figure 3. Schematic of axisymmetric flow field simulation.

IV. Numerical Accuracy

The steady flow field simulations in this paper were computed using a 5^{th} order finite difference stencil. For each case the grid was doubled in the streamwise and wall-normal directions until the solution was determined to be grid independent. Moreover, each simulation was computed until the error in the pressure field over 100k steps was less than 10^{-9} (i.e $O(\varepsilon_P) < 10^{-9}$).

A. Perfect Gas DNS

Figure 4 features the steady flow field wall-normal grid point comparison for Case C. The comparison location is near the cone tip where the velocity, density, pressure and temperature profiles have gradients across the entire shock layer and are not limited to the boundary layer. For all of the perfect gas cases the grid was doubled in the streamwise and wall-normal direction, however the streamwise grid density is known to be less critical and the figures are omitted. The profiles in Fig. 4 were doubled from 60 points to 120 points in the wall-normal direction to determine if the solution was grid-independent. As seen in Fig. 4a, the velocity and density profiles show no visible difference before and after grid doubling, the same is true of the pressure and temperature profiles seen in Fig. 4b. This indicates that 60 points is sufficient to accurately resolve the

solution, and that 120 is more than enough. Similarly, the perfect gas Cases A and B were also evaluated for grid convergence in this manner, and all three perfect gas cases were computed until their pressure field error was less than 10^{-9}.

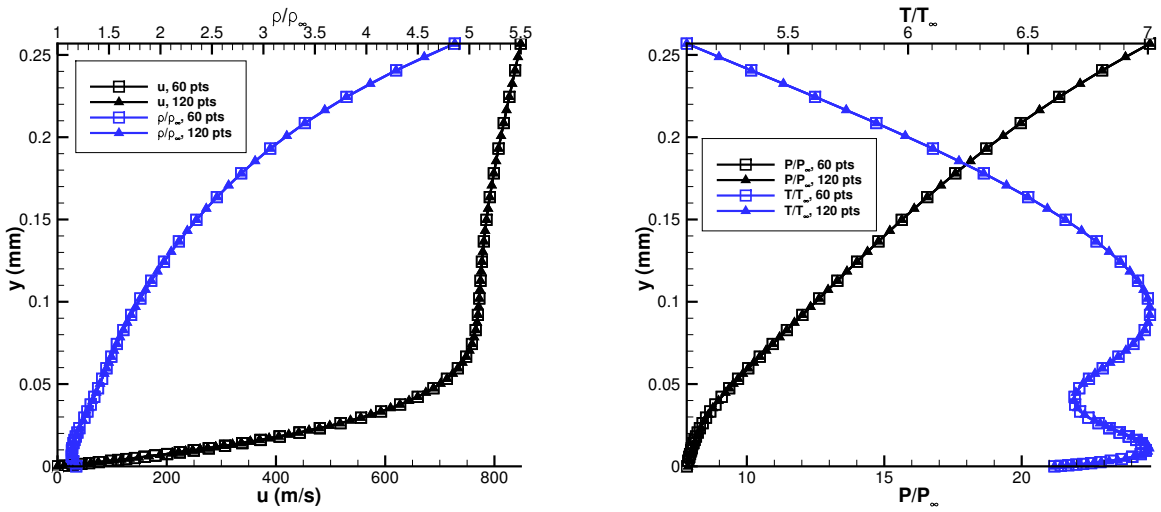

(a) (b)

Figure 4. Wall-normal grid point comparison of Case C mean flow boundary layer profiles at $s = 0.72$ mm. (a) u, and ρ/ρ_∞. (b) P/P_∞, and T/T_∞.

B. Thermochemical Nonequilibrium DNS

The steady flow field grid points in the wall-normal direction for thermochemical nonequilibrium Case 1 were doubled to 512 points from 256 to determine the number of grid points required for a grid-independent solution. Because Case 1 uses the same numerical methods and similar free stream conditions, a grid-independent resolution for Case 1 implies a grid-independent resolution for the remaining nonequilibrium cases. The wall-normal grid density is known to be much more critical than the wall-tangent grid density. In the wall-tangent direction, 5 grid points per millimeter are used and have been demonstrated to provide sufficient resolution.[20,21,29] Mean flow boundary layer profiles at $s = 0.4$ m (Fig. 5) indicate very little difference in the mean flow profiles when the grid is doubled. Furthermore, doubling the grid for the steady flow field solution significantly increased the computational expense to obtain a converged solution. Therefore, 256 grid points in the wall-normal direction was sufficient to provide an accurate solution.

V. Results: Perfect Gas

A. Case A: $M_\infty = 4.96$, Perfect Gas

Case A's steady flow field comes from the simulation of a blunt hypersonic cone at freestream conditions obtainable in Sandia National Laboratory's (SNL) hypersonic wind tunnel (HWT).[30] The high-order simulation of the flow field permits τ_w and $\dot{q}$ to be computed directly from the simulation, resulting in values for c_f and St along the length of the cone. Moreover, the boundary layer edge conditions along the cone were used to compute the laminar and turbulent correlations for c_f and St. Additionally, the freestream conditions were used to compute the Taylor-Maccoll solution for a flow over a supersonic cone. The surface values of the solution were in turn used to compute the laminar and turbulent correlations for c_f and St. Thus the utility of the correlations can be evaluated between a high-order but computationally expensive simulation, and a simplified but computationally cheap analytical solution.

As seen in Fig. 6, the laminar correlations based on the high-order simulation data are in very good agreement with the c_f and St calculated directly from the simulation; especially downstream of the nose. This suggests that the correlation accurately accounts for the behaviors of the velocity gradient and temperature

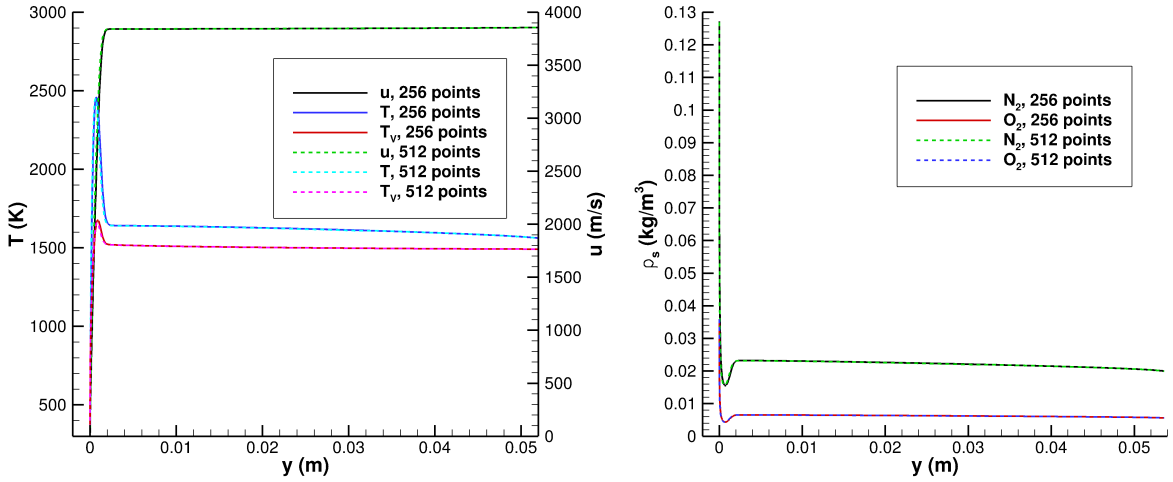

(a) (b)

Figure 5. Wall-normal grid point comparison of Case 1 mean flow boundary layer profiles at $s = 0.4$ m. (a) u, T, and T_V. (b) Species density ρ_s of N_2 and O_2 species.

gradient used in the direct calculation of c_f and St (see Eqs. 2 and 3). This result is not unexpected, as the simulation is 5th order accurate—and thus accounts for the behavior of the entire flow field—and there is no reason to doubt the validity of the correlation.

The same, however, cannot be said for the correlations based on the Taylor-Maccoll solution, which underpredicts c_f and St for both the laminar and turbulent calculations. This underprediction is due to the fact that the Taylor-Maccoll solution does not account for the boundary layer region and therefore the gradients $\frac{du}{dy}\Big|_{y=0}$ and $\frac{dT}{dy}\Big|_{y=0}$ are not accurately represented in the solution.

The dependency of c_f and St on $\frac{du}{dy}\Big|_{y=0}$ and $\frac{dT}{dy}\Big|_{y=0}$ is reinforced when both pairs of correlations are considered in the vicinity of the nose, where they differ significantly from the high-order simulation. This suggest that the validity of the correlations may become erroneous when $\frac{du}{dy}\Big|_{y=0}$ and $\frac{dT}{dy}\Big|_{y=0}$ are high. The disagreement between the correlations and simulation could also be because the correlations do not account for nose bluntness.

Since the high-order simulation is for a laminar mean flow, this study does not have a fully turbulent simulation to compare with the turbulent correlations. But since the simulation's laminar correlations are in good agreement with the simulation's direct calculation of c_f and St, the turbulent correlations are presumed to be a reasonable representation of c_f and St in a fully turbulent flow under the same freestream conditions. Again, the Taylor-Maccoll turbulent correlations underpredict the turbulent correlation based on the simulation.

Integrating the laminar and turbulent correlations over the body of the cone yield an approximation for the total skin drag, F_{skin}, and aerodynamic heat transfer rate, $\dot{Q}$. Figure 7 shows the skin drag and heat transfer rate for both the high-order simulation and Taylor-Maccoll results. Despite the Taylor-Maccoll correlations underpredicting c_f and St downstream, an overprediction in the vicinity of the nose is enough to produce a larger F_{skin} and $\dot{Q}$ for both laminar and turbulent correlations than the high-order simulation. Regardless, the laminar and turbulent results are in close agreement between the high-order simulation and Taylor-Maccoll. Physically, what can be seen from Fig. 7 is that the drag and heat transfer rate are significantly higher in the turbulent regime. In fact, at the end of the 0.5 meter long cone, the turbulent skin drag is over 2.8 times the laminar skin drag and the turbulent heating rate is over 3.4 times the laminar heating rate.

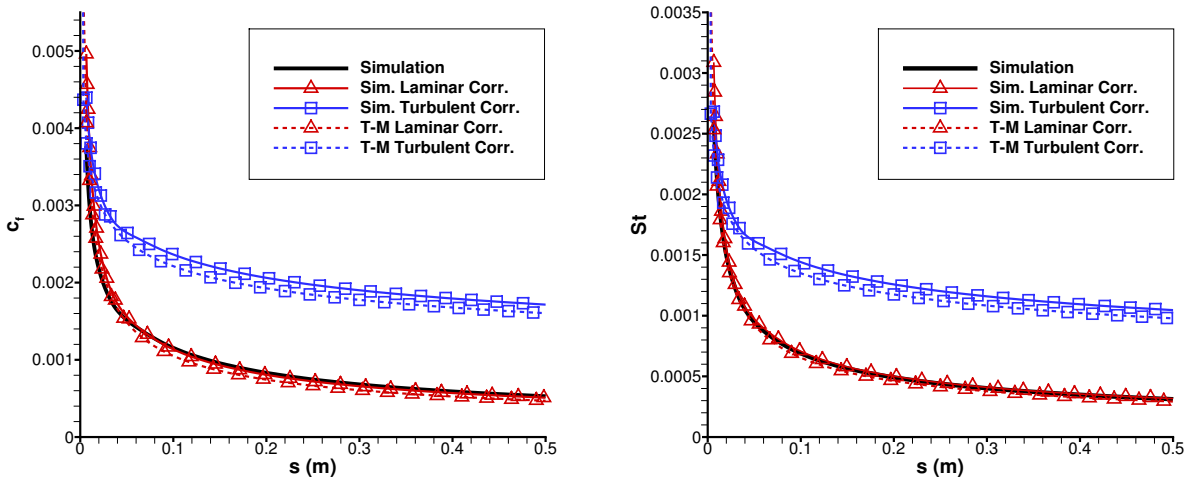

(a) (b)

Figure 6. Case A ($M_\infty = 4.96$, Perfect Gas) simulation vs. laminar and turbulent correlations. (a) Skin friction coefficient, c_f. (b) Stanton number, St.

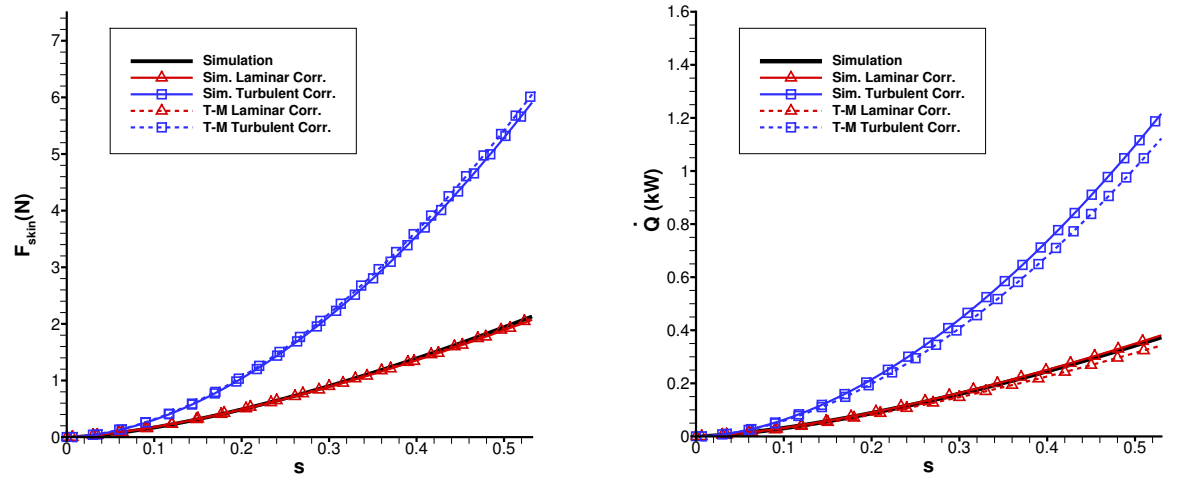

(a) (b)

Figure 7. Case A ($M_\infty = 4.96$, Perfect Gas) drag and heat transfer rate from laminar and turbulent correlations. (a) Total skin drag, F_{skin}. (b) Aerodynamic heat transfer rate, $\dot{Q}$.

B. Case B: $M_\infty = 7.84$, Perfect Gas

Case B's freestream parameters also come from conditions obtainable in SNL's HWT. One aspect of Case B that differs significantly from Case A and C is its sharper nose radius, $r_n = 0.05$ mm, which is ten times smaller than either perfect gas case, and is the sharpest nose radius of any of the cases considered in this paper. The effect of the sharpness is the near exactness of c_f and St between the simulation and its laminar correlation, especially in the vicinity of the nose as seen if Fig. 8. The reason for this agreement is thought to be the minimization of bluntness effects on the thermal and velocity boundary layers. This leads to the conclusion that the sharper the cone is the more accurate the correlations are. Again, there is no data to compare the turbulent correlations with, but still there is no reason to doubt its validity.

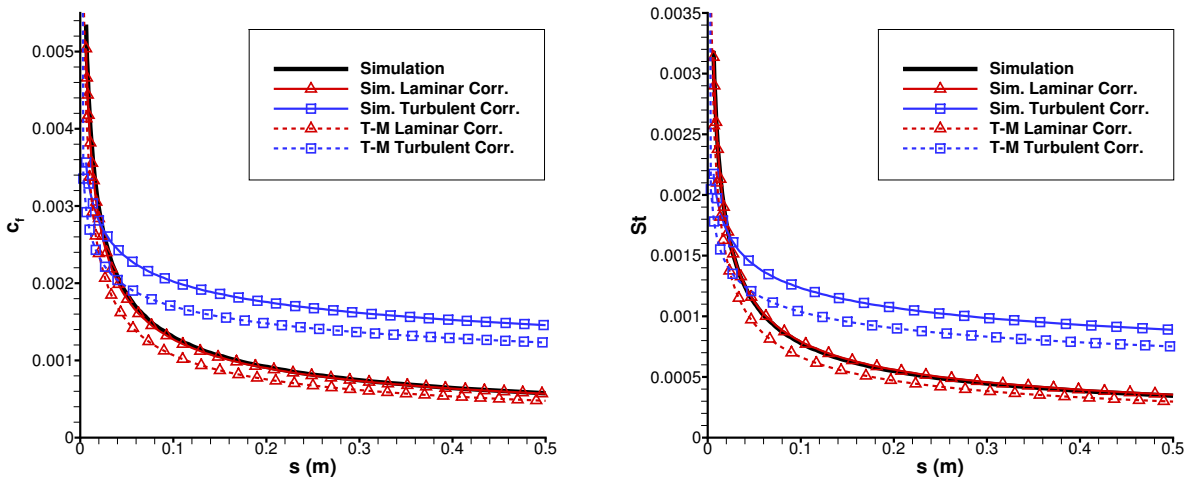

(a) (b)

Figure 8. Case B ($M_\infty = 7.84$, Perfect Gas) simulation vs. laminar and turbulent correlations. (a) Skin friction coefficient, c_f. (b) Stanton number, St.

With respect to the Taylor-Maccoll solution, as seen in Fig. 8, it appears that the correlations still underestimate c_f and St, only now the underestimations appear to increase with increasing Mach number. This does not bode well for the computationally less-intensive Taylor-Maccoll approach. This in an inconvenient trend if one is using the Taylor-Maccoll solution to characterize laminar and turbulent hypersonic boundary layers.

On the other hand, when the correlations for both solution sets are integrated over the cone, their results for F_{skin} and $\dot{Q}$ are in close agreement with one another as seen in Fig. 9. For this higher Mach number case, at the end of the cone the turbulent skin drag is nearly twice that of the laminar skin drag, and the turbulent heat transfer rate is nearly 2.3 times the laminar heat transfer rate. Compared with Case A, the relative increase from laminar to turbulent at the end of the cone is not nearly as high. Comparing the absolute values, however, is a different story. The laminar F_{skin} in Fig. 7 and 9 are nearly the same for the two cases, however, the turbulent F_{skin} is significantly higher for the Mach 4.96 case. Moreover, the laminar and turbulent values for $\dot{Q}$ are higher for Case B than Case A.

C. Case C: $M_\infty = 8$, Perfect Gas

The last of the perfect gas cases considered in the paper is Case C. As with the previous two cases, the freestream parameters come from conditions obtainable in SNL's HWT. Case C is included in this study because it has the same nose radius as Case A and nearly the same Mach number as Case B. Thus, the effect of nose bluntness and Mach number on the correlations can be qualitatively characterized independently.

Figure 10 shows that the agreement between the high-order simulations and its laminar and turbulent correlations is still in great agreement with some discrepancy in the nose region due to bluntness. Moreover, the Taylor-Maccoll solution correlations still underpredict the high-order simulation solution as a result of

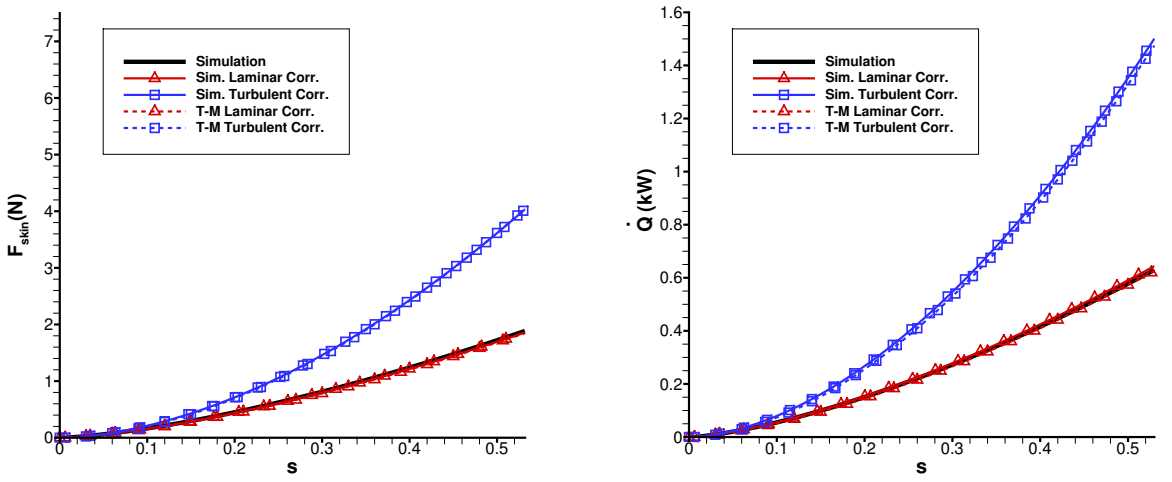

(a) (b)

Figure 9. Case B ($M_\infty = 7.84$, Perfect Gas) drag and heat transfer rate from laminar and turbulent correlations. (a) Total skin drag, F_{skin}. (b) Aerodynamic heat transfer rate, $\dot{Q}$.

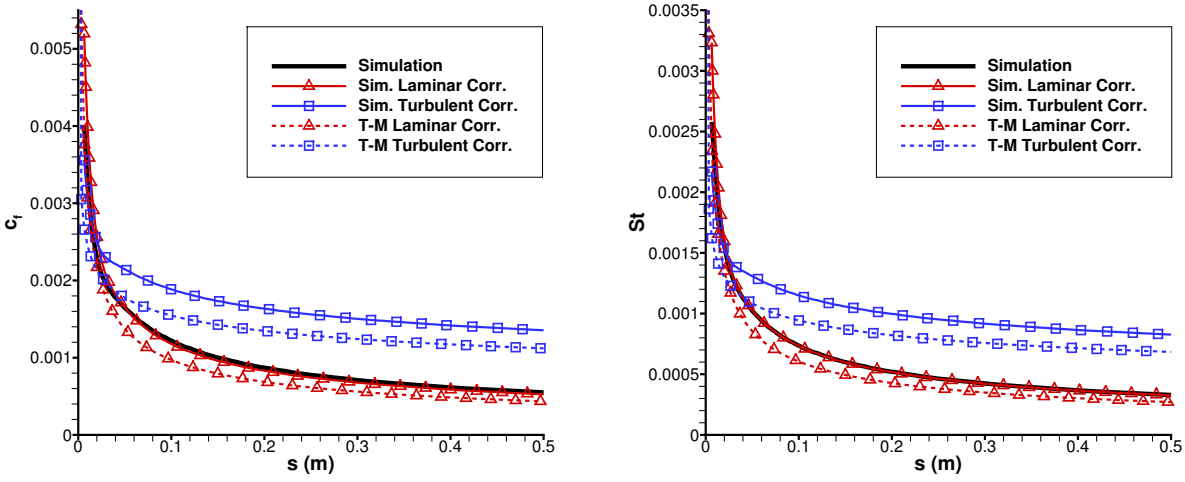

(a) (b)

Figure 10. Case C ($M_\infty = 8$, Perfect Gas) simulation vs. laminar and turbulent correlations. (a) Skin friction coefficient, c_f. (b) Stanton number, St.

the higher Mach number. Unsurprisingly, there is little change in the F_{skin} and $\dot{Q}$ results seen in Fig. 11 over those seen in Fig. 9 for Case B because their free stream Mach numbers are nearly equal.

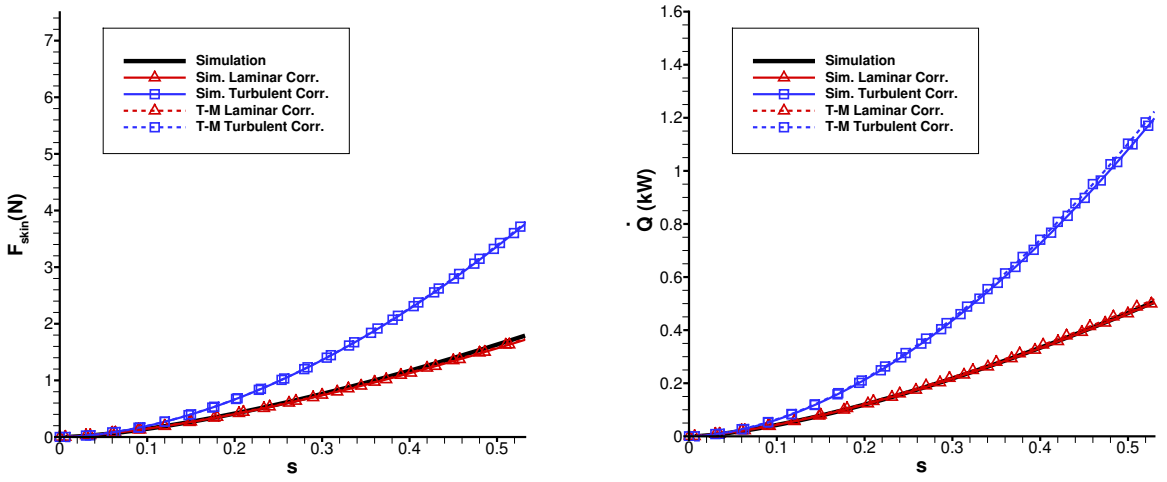

(a) (b)

Figure 11. Case C ($M_\infty = 8$, Perfect Gas) drag and heat transfer rate from laminar and turbulent correlations. (a) Total skin drag, F_{skin}. (b) Aerodynamic heat transfer rate, $\dot{Q}$.

D. Impact of Transition Location on Drag and Heating

Because the drag and heating results in Figs. 7, 9 and 11 assume fully laminar or fully turbulent flow over the entire length of the body, neither result is particularly realistic or useful. In general, the boundary layer will transition from laminar to turbulent at a location that is a function of the freestream parameters, geometry, surface conditions, etc. Because there is no theory to predict the transition location and it is typically obtained from experiment, the transition location, s_{tr} is parametrically varied over the length of the cone to determine the impact on skin drag and surface heating. For this analysis the laminar and turbulent correlations utilizing the high-order simulation data are used (the Taylor-Maccoll correlations are not featured). Fig. 12 shows the total skin drag force at the end of the 0.5 meter cone as a function of the transition location, s_{tr}. Fig. 12a presents the data in dimensional units (Newtons of force), Fig. 12b presents the data as percent reduction in drag force compared to the fully turbulent flow, and Fig. 12c presents the data as percent increase in drag force compared to what percent of the boundary layer is turbulent, with 0% being fully laminar and 100% being fully turbulent. Theses figures demonstrate the importance of predicting or delaying hypersonic boundary layer transition.

For Case A, if transition can be delayed the length of the cone, there is an over 64% reduction in skin drag compared to a fully turbulent flow. Alternatively, if transition occurs immediately, there is a 185% increase in skin drag compared to the fully laminar case. In a hypothetical scenario, where transition occurs naturally at $s_{tr} = 0.3$ m and is delayed 10 cm to 0.4 m, the total drag is reduced from 4.7 N to 3.75 N: a 20% reduction in drag. Likewise for Case B and C, if laminar flow is maintained over the length of the cone, there is a nearly 54% reduction in skin drag over a fully turbulent flow. If transition were to occur immediately, there is an approximately 118% increase in skin drag. Similarly in the same hypothetical scenario, if transition were to occur naturally at $s_{tr} = 0.3$ m and is delayed to 0.4 m, the total drag is reduced from approximately 3.27 N to 2.7 N: a 17% reduction in drag. These scenarios show that significant reductions in skin drag are obtainable with only a modest delay in transition. How beneficial the reduction actually is, however, depends on where transition occurs, how far it can be delayed, and the slope of F_{skin}.

The impact of transition location on aerodynamic heating is also examined and presented in Fig. 13. The transition location has a similar impact on heating rate as skin drag. For Case A, if transition can be delayed beyond the end of the cone, there is an over 68% reduction in heat transfer rate compared to the fully turbulent case. Alternatively, if transition occurs immediately, there is a 219% increase in heating

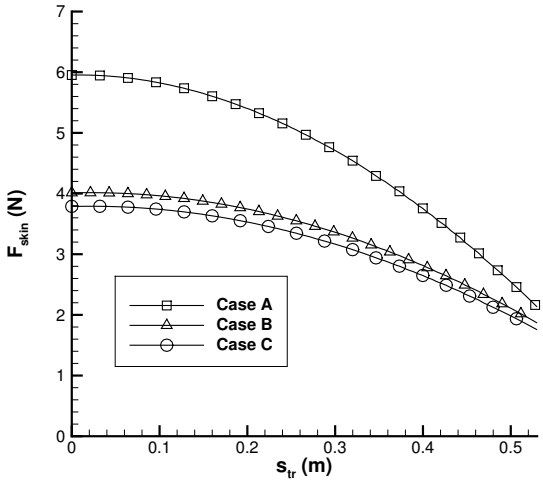

(a)

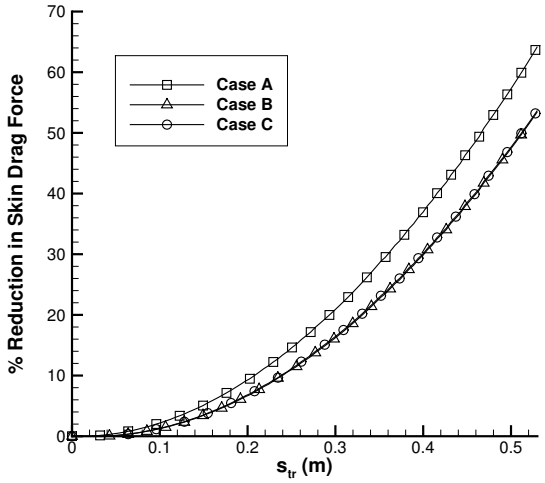

(b)

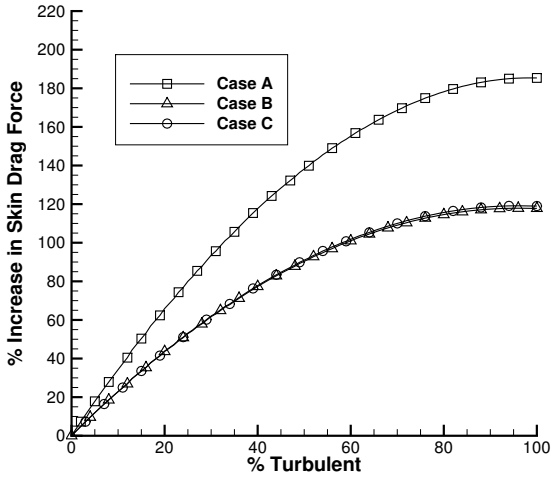

(c)

Figure 12. Case A ($M_\infty = 4.96$, Perfect Gas) total skin drag, F_{skin}, as a function of transition location, s_{tr}. (a) Dimensional units. (b) Percent reduction in drag compared to fully turbulent flow. (c) Percent increase in drag compared to fully laminar flow.

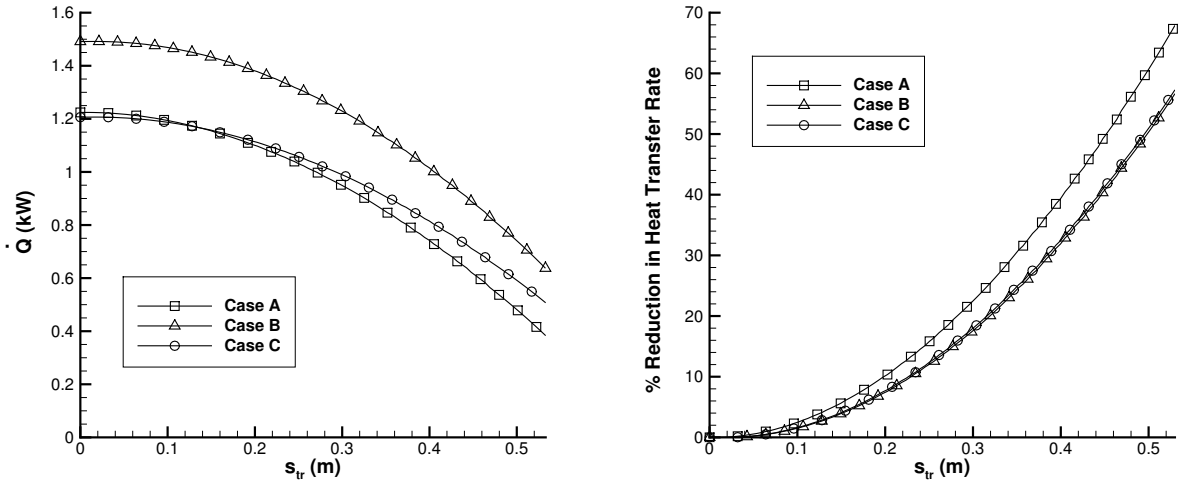

(a)

(b)

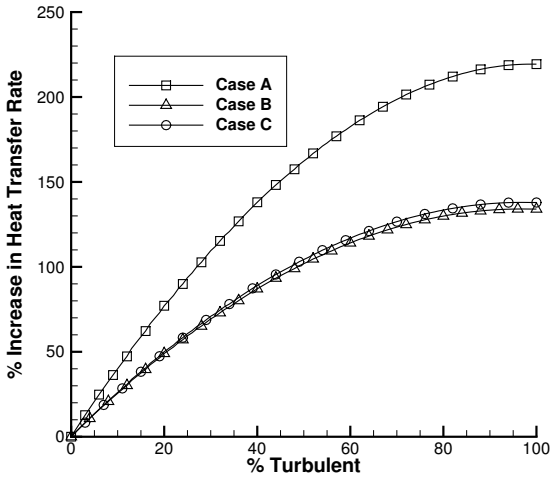

(c)

Figure 13. Case A ($M_\infty = 4.96$, Perfect Gas) total aerodynamic surface heating rate, $\dot{Q}$, as a function of transition location, s_{tr}. (a) Dimensional units. (b) Percent reduction in heating rate compared to fully turbulent flow. (c) Percent increase in heating rate compared to fully laminar flow.

rate compared to the fully laminar case. Again invoking the hypothetical example, delaying transition from $s_{tr} = 0.3$ m to 0.4 m causes a decrease in heat transfer rate from 0.95 kW to 0.74 kW: a 22% reduction in aerodynamic heating. Likewise for Case B and C, if laminar flow is maintained over the length of the cone, there is an nearly 57% reduction in heat transfer rate over a fully turbulent flow. And, if transition were to occur immediately, there is an approximately 136% increase in heat transfer rate. Similarly in the hypothetical scenario, if natural transition were delayed, the heat transfer rate is reduced from approximately 1.1 kW to 0.9 kW: an 18% reduction in drag. These scenarios further demonstrate that significant reductions in surface heat transfer rates are also obtainable with a modest delay in transition. But once again are dependent on where transition naturally occurs, how far it can be delayed and the slope of $\dot{Q}$.

It should be noted that the magnitude of skin drag force and heat transfer rate are quite small for all the perfect gas cases. This is likely due to a number of factors. First, the cone is very short; only 0.5 meters in length. Second, the freestream gas density is very small, on the order of 10^{-2}, resulting in a low gas inertia. In practice, more realistic longer geometries with blunter nose radii in atmospheric conditions will have significantly higher absolute drag and heating values.

VI. Results: Nonequilibrium Gas

A. Comparison of Correlations with DNS and Taylor-Maccoll Solution

The laminar and turbulent correlations for c_f and St at each streamwise location were computed using the boundary layer edge conditions computed by DNS and the Taylor-Maccoll analysis. The comparison between the simulation and laminar and turbulent correlations for Case 1 is shown in Fig. 14, with Case 2, 3, and 4 shown in Figs. 15, 16, and 17, respectively. The Case 1 Taylor-Maccoll boundary layer edge conditions (Fig. 14) agree very closely with the laminar correlations for both c_f and St using the boundary layer edge variables extracted from DNS, however the laminar correlations slightly over-predict c_f and St computed directly from the simulation. There is a very large discrepancy for the turbulent correlations for both c_f and St, however. The correlations using DNS boundary layer edge conditions predict a significantly higher c_f and St than those using the Taylor-Maccoll solution. Similar trends are encountered for Case 2 (Fig. 15); the laminar correlations for c_f and St agree well between the simulation edge conditions and the Taylor-Maccoll edge conditions, while the turbulent correlations have a large discrepancy. However, the Case 2 laminar correlations for c_f appear to agree better with the c_f computed directly from the simulation, while the St correlations under-predict the simulation St.

There is also good agreement for Case 3 (Fig. 16) between the c_f and St correlations using DNS edge conditions and the c_f and St computed directly from the simulation. However, the correlations using the Taylor-Maccoll edge conditions under-predict the correlations using simulation edge conditions. The laminar correlation closely follows the simulation for c_f, although there is a slight under-prediction of both c_f and St by the laminar correlation. Lastly, Case 4 shows similar trends (Fig. 17) as Case 3. The laminar correlation using simulation edge conditions closely follows the simulation for c_f, although there is a slight over-prediction of both c_f and St by the laminar correlation; a similar trend as the cold-wall Case 1. Again, the correlations using Taylor-Maccoll edge conditions significantly under-predict both c_f and St for laminar and turbulent flow. Possible explanations for the discrepancies between the simulations and the correlations are addressed in the Conclusions section. In general, however, the laminar correlations provide a reasonable estimate of c_f and St for all nonequilibrium cases, although there is a clear sensitivity of the turbulent correlations to boundary layer edge conditions, whereas the laminar correlations are not as sensitive.

B. Laminar and Turbulent Drag and Surface Heating Rate

Because the laminar correlations using the edge conditions from DNS in Figs. 14-17 were in reasonable agreement with the simulation, one can extrapolate that the turbulent correlation would provide a reasonable agreement to turbulent flow under these free stream conditions as well. Furthermore, experimental results support the turbulent correlations used here.[31] Integrating the laminar and turbulent correlations over the body of the cone would then yield an approximation for the total skin drag, F_{skin}, and aerodynamic heat transfer rate, $\dot{Q}$. The skin drag force and heating rate from the simulation were compared to the laminar and turbulent correlations obtained using both the simulation boundary layer edge conditions and the Taylor-Maccoll edge conditions. The comparison of the drag from the simulation and correlations for Cases 1, 2, 3, and 4 are shown in Figs. 18a, 19a, 20a, and 21a, respectively. The corresponding surface heating rates are

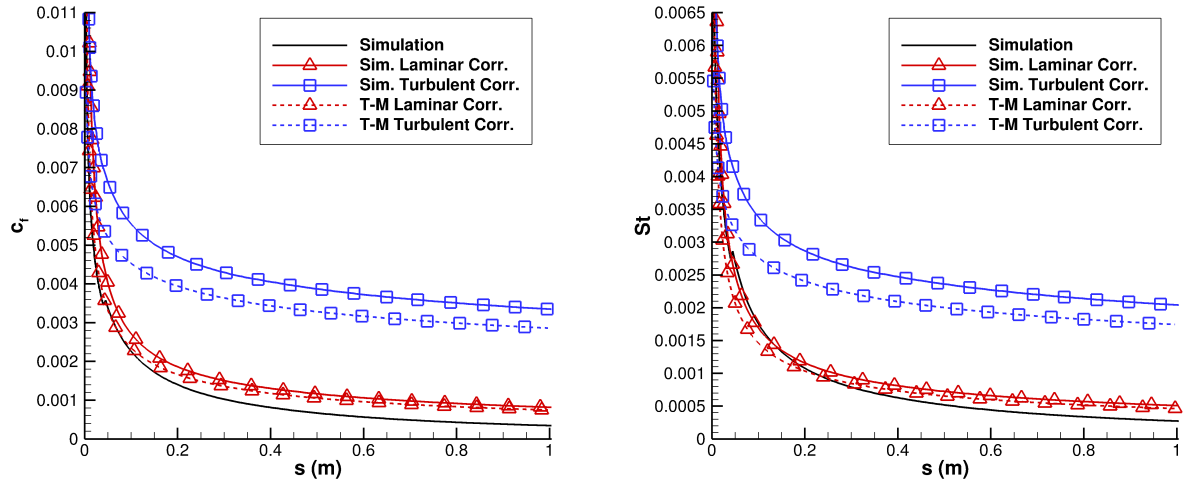

(a) (b)

Figure 14. Case 1 ($M_\infty = 5$, Nonequilibrium, Cold Wall) simulation vs. laminar and turbulent correlations computed using DNS boundary layer edge variables and axisymmetric shock solution (T-M). (a) Skin friction coefficient, c_f. (b) Stanton number, St.

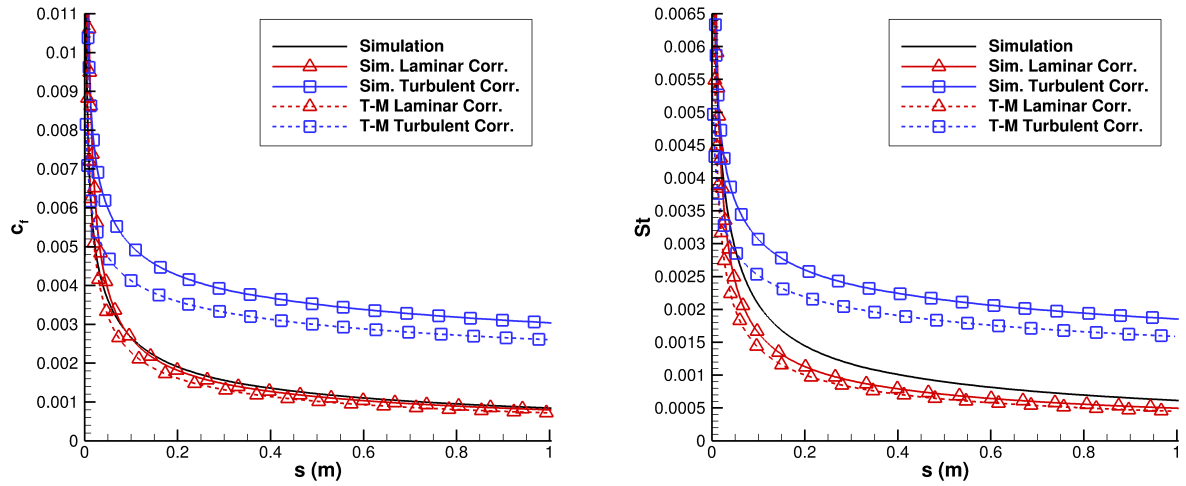

(a) (b)

Figure 15. Case 2 ($M_\infty = 5$, Nonequilibrium, Warmer Wall) simulation vs. laminar and turbulent correlations computed using DNS boundary layer edge variables and axisymmetric shock solution (T-M). (a) Skin friction coefficient, c_f. (b) Stanton number, St.

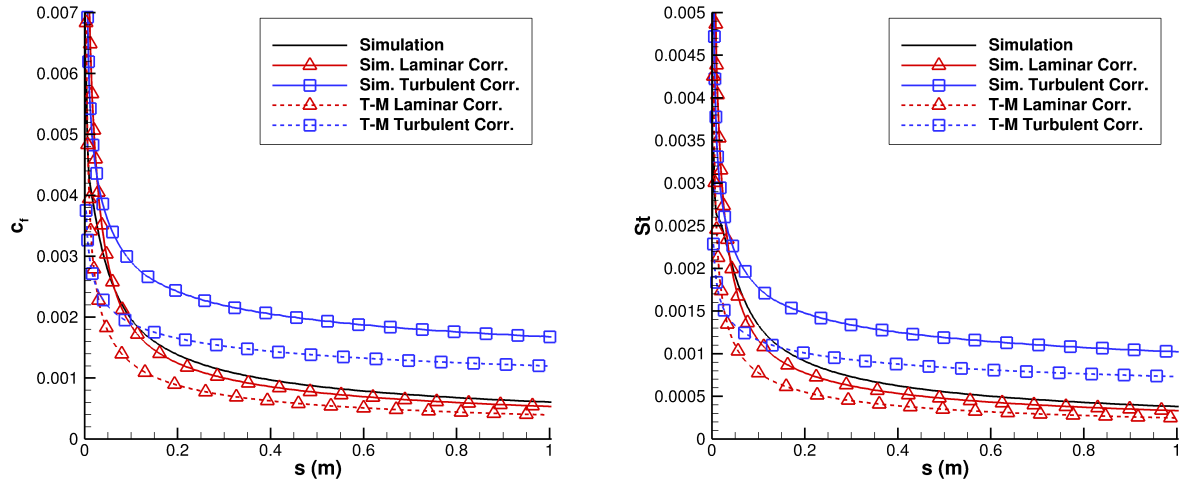

(a) (b)

Figure 16. Case 3 ($M_\infty = 10$, Nonequilibrium, Hot Wall) simulation vs. laminar and turbulent correlations computed using DNS boundary layer edge variables and axisymmetric shock solution (T-M). (a) Skin friction coefficient, c_f. (b) Stanton number, St.

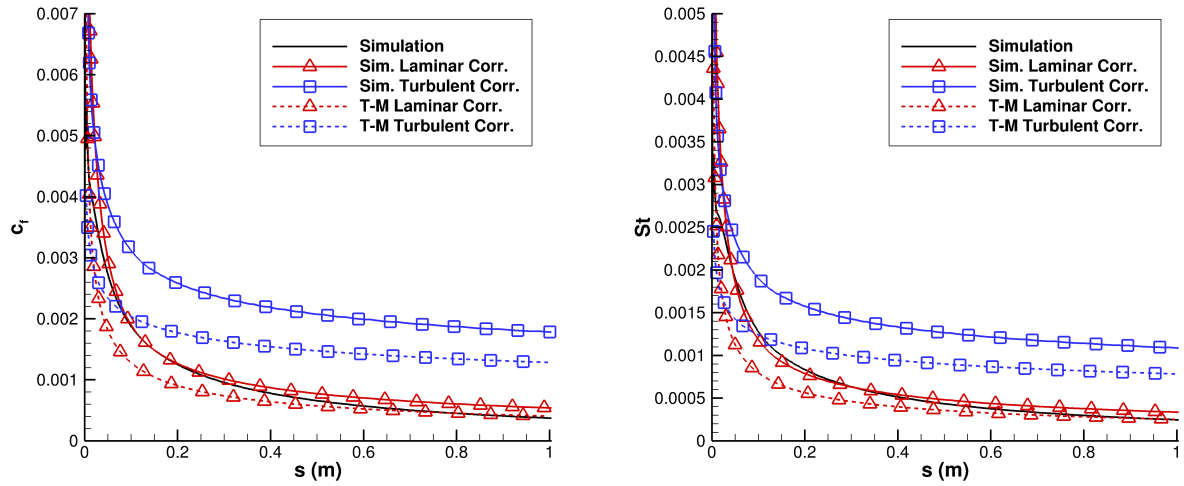

(a) (b)

Figure 17. Case 4 ($M_\infty = 10$, Nonequilibrium, Cold Wall) simulation vs. laminar and turbulent correlations computed using DNS boundary layer edge variables and axisymmetric shock solution (T-M). (a) Skin friction coefficient, c_f. (b) Stanton number, St.

shown in Figs. 18b, 19b, 20b, and 21b, respectively. Collectively a number of trends can be seen. First, the choice of boundary layer edge conditions seems to have only a small impact on total drag for both laminar and turbulent correlations. There is slightly greater variation in surface heating rate depending on the edge condition for the correlations, however. Second, both laminar correlations reasonably follow the computed drag and heating from DNS, with the greatest deviation occurring in Case 1. Third, the laminar correlations for the cold wall flows (Cases 1 and 4 in Figs. 18 and 21, respectively) over-predict the laminar drag and heating from DNS. The correlations for warmer wall flows (Cases 2 and 3 in Figs. 19 and 20, respectively) more accurately follow the simulation drag and heating, yet show a small under-prediction.

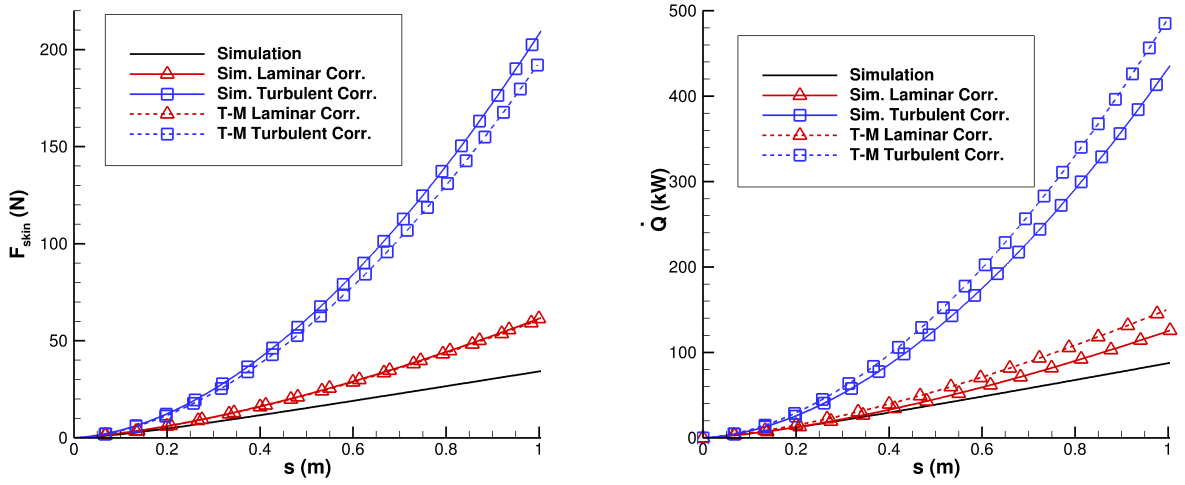

(a) (b)

Figure 18. Case 1 ($M_\infty = 5$, Nonequilibrium, Cold Wall) drag and heat transfer rate from simulation compared to laminar and turbulent correlations. (a) Drag, F_{skin}. (b) Aerodynamic heat transfer rate, $\dot{Q}$.

Lastly, all correlations using the DNS boundary layer edge conditions are directly compared in Fig. 22. Most notable is the similarity between skin drag force between all cases (Fig. 22a). Despite the Mach number between Cases 1/2 and 3/4 doubling, there is only a small increase in drag force in both laminar and turbulent flow. Consistent for all cases, however, is the drastic increase in drag for turbulent flow: nearly a four-fold increase in skin drag force. The surface heating rates (Fig. 22b) show significantly more variation between cases, however. Case 2 shows the lowest heat transfer for both laminar and turbulent flow. This is intuitive because it is the lowest Mach number flow with a warmer wall than Case 1. Because Case 1 had a colder wall than Case 2 (with the same free stream conditions), Case 1 had slightly higher heat transfer rates. Cases 3 and 4 had even higher $\dot{Q}$ due to the increase in Mach number and free stream stagnation enthalpy. Following a similar trend, the colder wall Case 4 had more heat transfer than the warmer wall Case 3.

The results in Fig. 22 indicate that the skin drag force experienced by the vehicle is significantly increased in the turbulent regime, however there is little variation in drag as Mach number and wall temperature are changed. That is, the skin drag on the vehicle is not very sensitive to the free stream parameters or surface temperature. The surface heating rate, however, shows much more sensitivity to these parameters. Higher-enthalpy flows with colder walls experienced noticeably more heat transfer than the lower-enthalpy warmer wall flows. These results show that heat transfer rate, rather than skin drag force, is the critical design parameter in predicting boundary layer transition in hypersonic flight.

C. Impact of Transition Location on Drag and Heating

Because the drag and heating results in Fig. 22 assume fully laminar or fully turbulent flow over the entire length of the body, neither result is particularly realistic. Predicting the transition location from laminar to turbulent is not straightforward, the transition location, s_{tr} is varied numerically over the length of the cone to determine the impact on skin drag and surface heating. Fig. 23 shows the impact of transition location

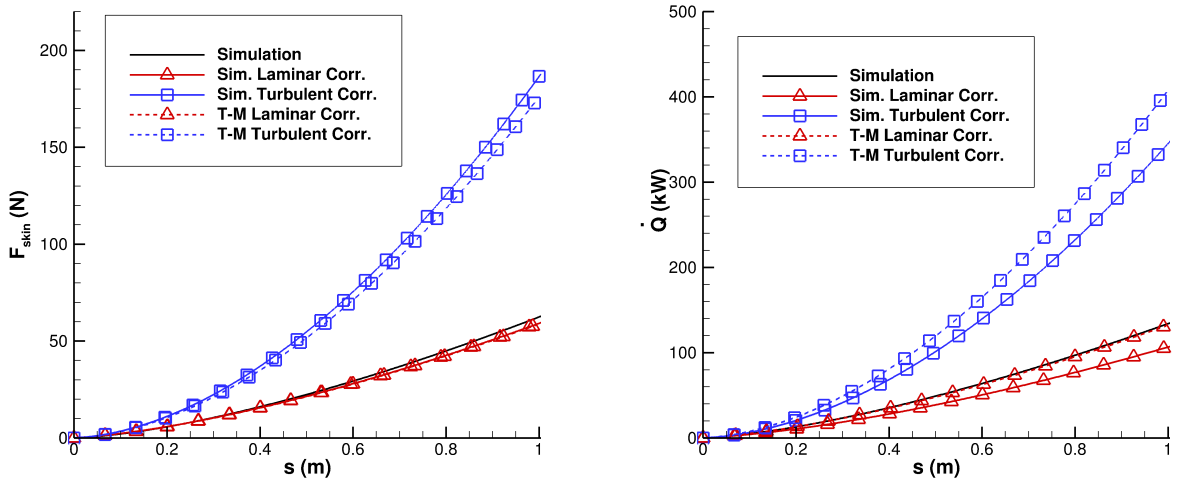

(a) (b)

Figure 19. Case 2 ($M_\infty = 5$, Nonequilibrium, Warmer Wall) drag and heat transfer rate from simulation compared to laminar and turbulent correlations. (a) Drag, F_{skin}. (b) Aerodynamic heat transfer rate, $\dot{Q}$.

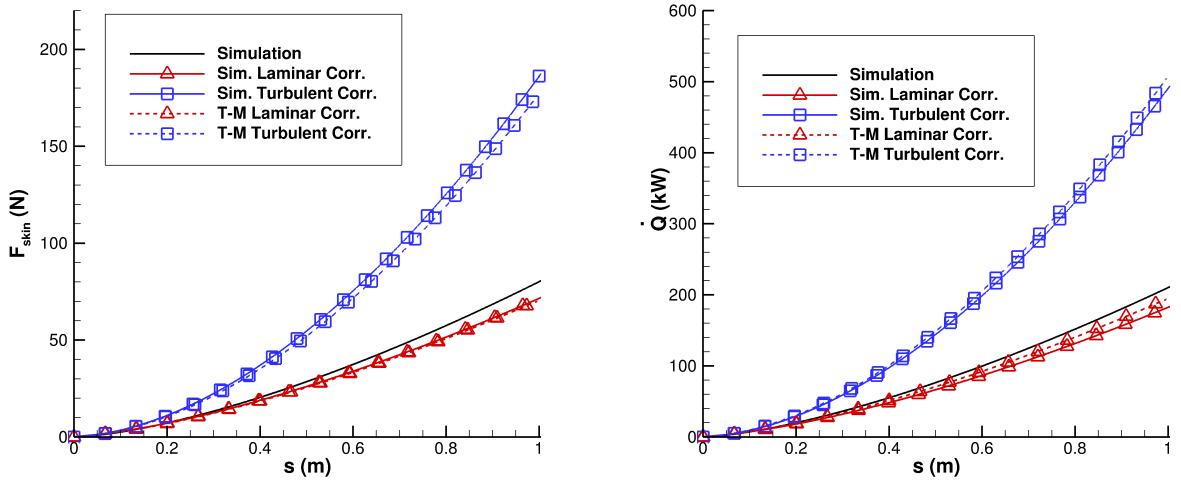

(a) (b)

Figure 20. Case 3 ($M_\infty = 10$, Nonequilibrium, Hot Wall) drag and heat transfer rate from simulation compared to laminar and turbulent correlations. (a) Drag, F_{skin}. (b) Aerodynamic heat transfer rate, $\dot{Q}$.

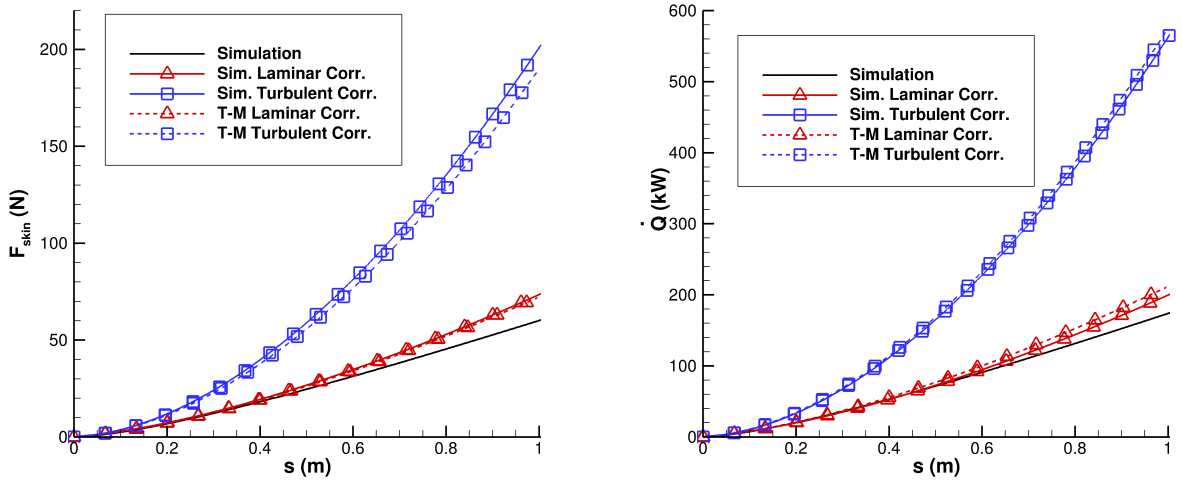

(a) (b)

Figure 21. Case 4 ($M_\infty = 10$, Nonequilibrium, Cold Wall) drag and heat transfer rate from simulation compared to laminar and turbulent correlations. (a) Drag, F_{skin}. (b) Aerodynamic heat transfer rate, $\dot{Q}$.

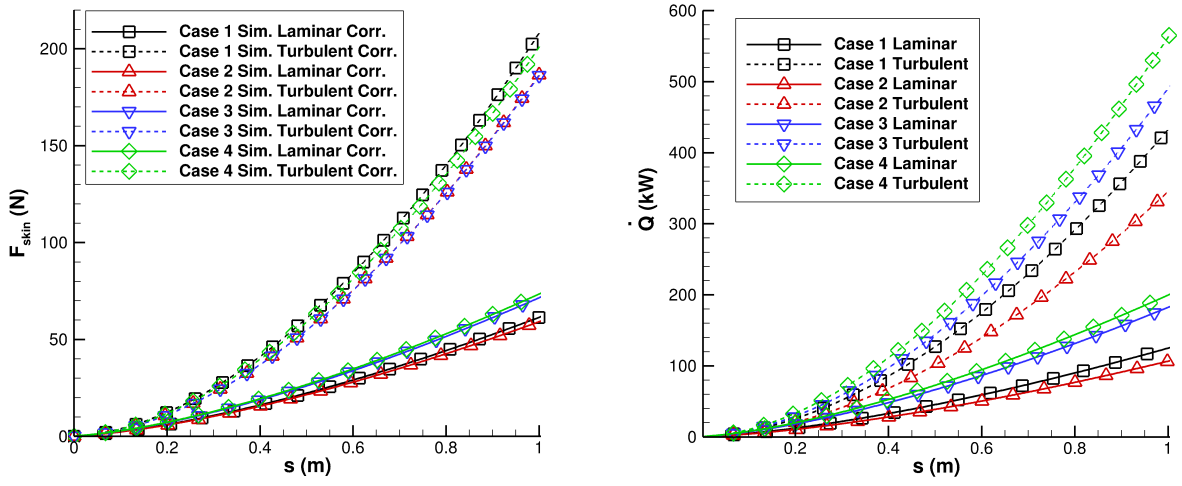

(a) (b)

Figure 22. Comparison of all nonequilibrium cases for total skin drag force, F_{skin}, and total aerodynamic surface heating rate, $\dot{Q}$, as a function of streamwise distance, s. (a) Skin drag force, F_{skin}. (b) Surface heating rate, $\dot{Q}$.

on total skin drag force at the end of the 1 meter long cone. Fig. 23a presents the data in dimensional units (Newtons of force), Fig. 23b presents the data as percent reduction in drag force compared to the fully turbulent flow, and Fig. 23c presents the data as percent increase in drag force as a function of the percent of the cone experiencing turbulent flow. If transition can be delayed beyond the length of the cone, the reduction in drag is between 60% and 70% compared to a fully turbulent flow (Fig. 23b). Alternatively, if transition occurs immediately on the cone, i.e. 100% turbulent flow, the increase in drag is between 150% and 230% compared to the fully laminar case (Fig. 23c). All nonequilibrium cases have similar laminar drag, but as s_{tr} approaches the leading edge of the cone, Cases 1 and 4 have higher magnitudes of drag force, while Cases 2 and 3 have nearly identical drag forces (Fig. 23a). In terms of percentages, however, the lower enthalpy Cases 1 and 2 have significantly greater percentage increase in drag compared to their respective fully laminar cases (Fig. 23c). Nevertheless, the magnitude of drag force is quite small for all cases and other sources of drag, e.g. pressure and wave drag, are more likely to dominate.

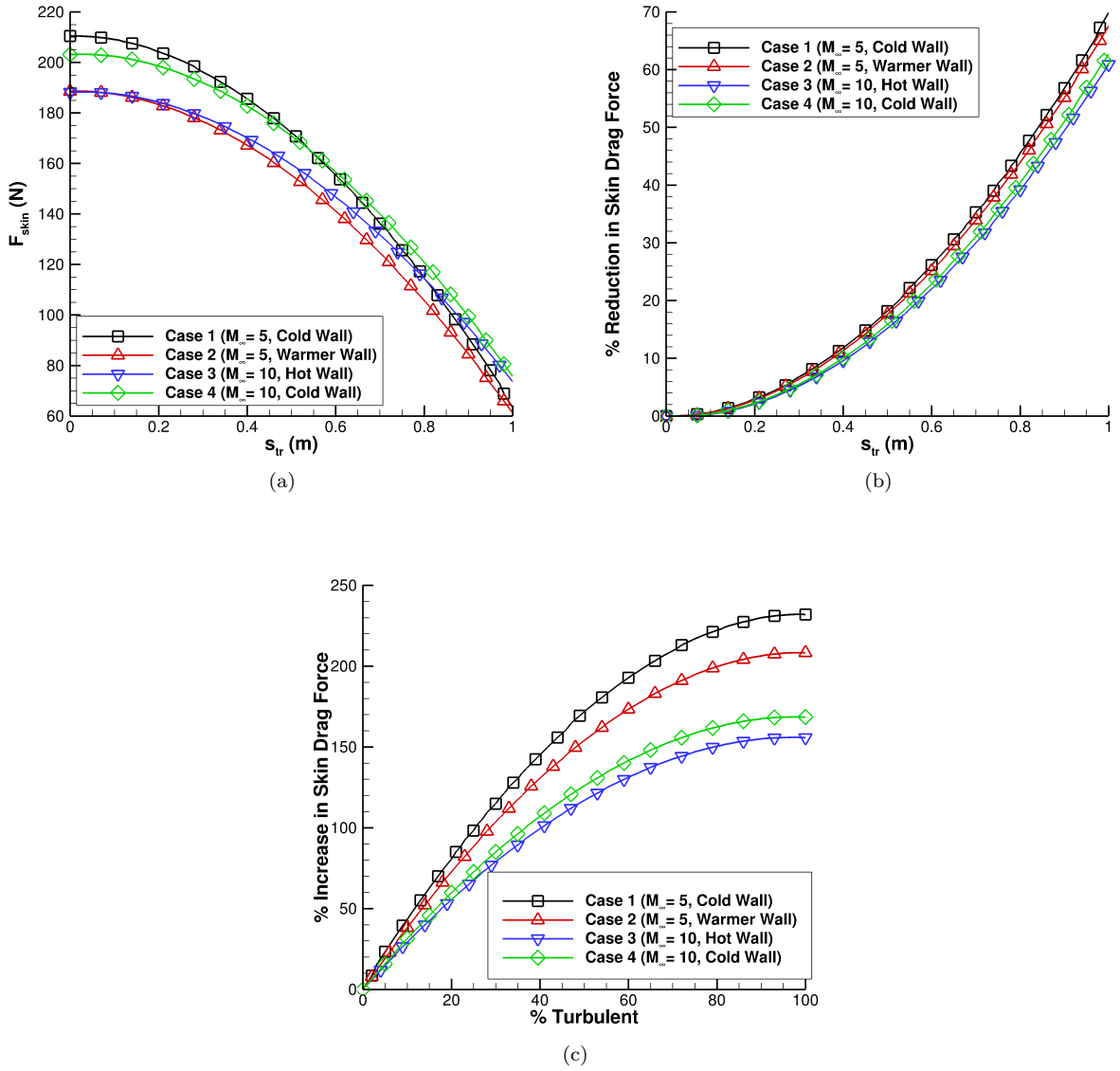

Figure 23. Comparison of impact of transition location on total skin drag force, F_{skin}, for nonequilibrium Cases 1-4. (a) Dimensional units. (b) Percent reduction in drag compared to fully turbulent flow. (c) Percent increase in drag as a function of the percent of the cone experiencing turbulent flow.

The impact of transition location on aerodynamic heating is also examined and presented in Fig. 24.

Fig. 24a presents the data in dimensional units (kW), Fig. 24b presents the data as percent reduction in heat transfer rate compared to the fully turbulent flow, and Fig. 24c presents the data as percent increase in heat transfer rate as a function of the percent of the cone experiencing turbulent flow. The transition location has a similar impact on heating rate as skin drag. If transition can be delayed beyond the end of the cone, the reduction in heating is between 60% and 70% compared to the fully turbulent case (Fig. 24b). Alternatively, if transition occurs immediately, the increase in heating is between 160% and 240% compared to the fully laminar case (Fig. 24c). The maximum magnitude of drag occurs in Case 4, followed by Case 3, Case 1, and Case 2 (Fig. 24a). This result shows that colder walls have higher heat transfer, and that higher enthalpy flows have higher heat transfer. In terms of percentages, however, the lower enthalpy Cases 1 and 2 have significantly greater percentage increase in heating compared to their respective fully laminar cases (Fig. 24c), while all cases have a similar reduction in heat transfer compared to their respective turbulent cases (Fig. 24b).

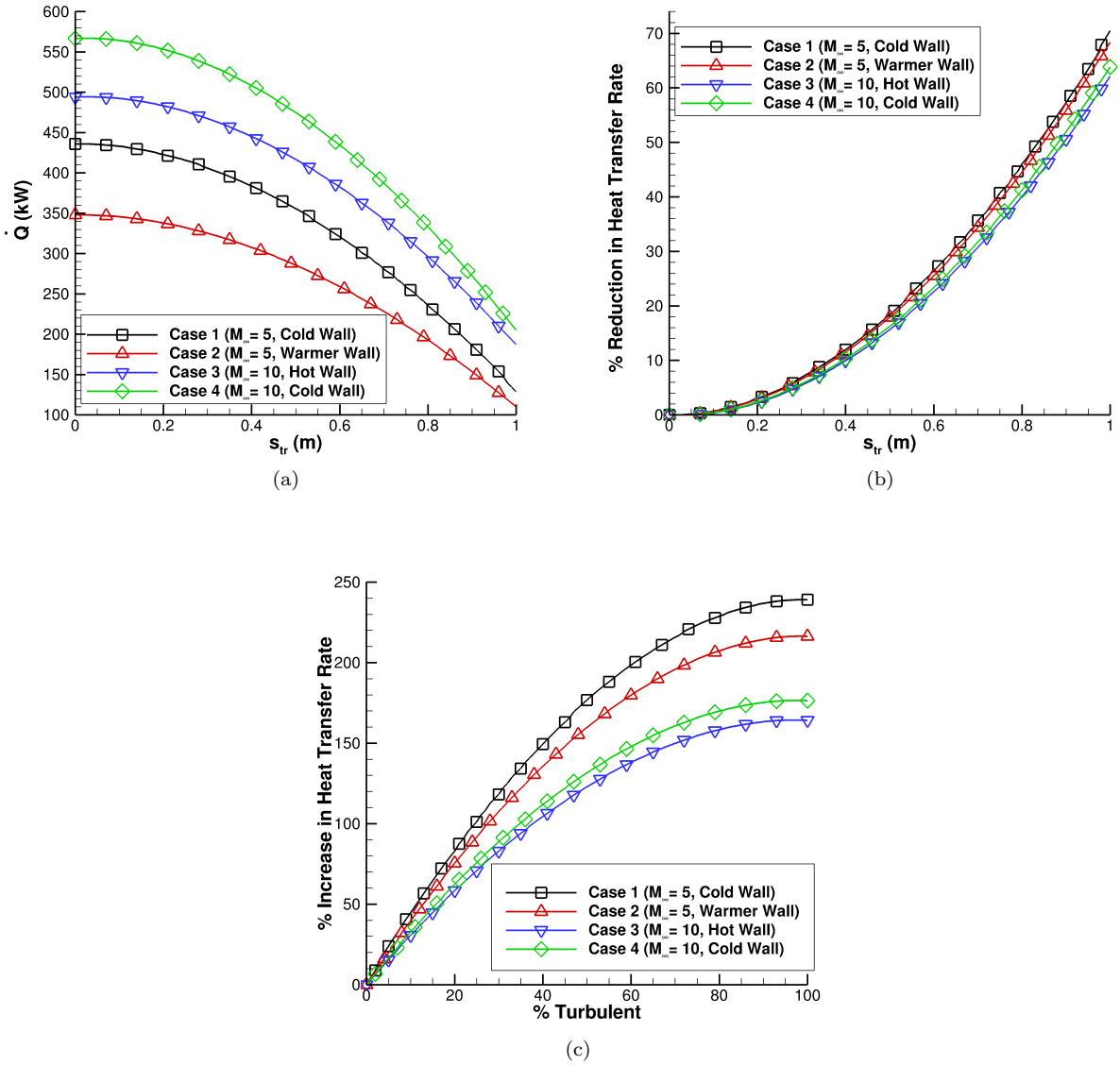

Figure 24. Comparison of impact of transition location on aerodynamic heat transfer rate, $\dot{Q}$, for nonequilibrium Cases 1-4. (a) Dimensional units. (b) Percent reduction in heating rate compared to fully turbulent flow. (c) Percent increase in heating rate as a function of the percent of the cone experiencing turbulent flow.

VII. Summary and Conclusions

Steady flow simulations obtained from DNS were used to compute the skin friction coefficient and Stanton number for seven hypersonic flow cases over a blunt cone. Three cases assumed a perfect gas model, with the remaining four cases including thermochemical nonequilibrium effects. The skin friction coefficient and Stanton number from the simulations were compared to laminar and turbulent correlations for the same parameters based on boundary layer edge conditions obtained from both the DNS simulation and from the Taylor-Maccoll axisymmetric shock solution, in which reasonable agreement was found. This agreement justified the accuracy of the laminar and turbulent correlations, which were subsequently used to compute the total skin drag force and aerodynamic surface heating rate for fully laminar and fully turbulent flow. The impact of the transition location was examined, and it was found that delaying transition by even a small distance could have a significant effect on drag and heating. Overall, it has been shown that accurately predicting or even delaying transition can have significant design implications in terms of skin drag and aerodynamic surface heating. Laminar flow was shown to have up to 70% lower skin drag and surface heat transfer rate than the fully turbulent case. Alternatively, turbulent flow was shown to have up to 230% higher skin drag and 240% higher heating rate compared to laminar flow.

A number of conclusions can be drawn about using the simplified correlations to study the impact of hypersonic boundary layer transition. First, although there were some discrepancies between the correlations and the DNS, the correlations still provided a reasonable estimate of drag and heating with the benefit of minimal computational cost. The best agreement between the laminar correlations and DNS was observed for the perfect gas, sharp nose cases. Furthermore, in the perfect gas simulations, the choice of boundary layer edge conditions (extracted from DNS or from the Taylor-Maccoll analysis) in the correlations resulted in only small differences in c_f and St, but when integrated over the surface of the cone to obtain total skin friction drag and heating rates, the Taylor-Maccoll edge conditions resulted in nearly identical results as the correlations using the DNS edge conditions. The most prevalent issue with the Taylor-Maccoll solutions is that it does not accurately represent $\left.\frac{du}{dy}\right|_{y=0}$ and $\left.\frac{dT}{dy}\right|_{y=0}$, especially when those wall gradients are particularly steep. However, using the Taylor-Maccoll analysis in conjunction with the laminar and turbulent correlations used here is likely satisfactory when computing estimates of laminar drag and heating on hypersonic cones with small nose radii under a perfect gas assumption.

For the nonequilibrium gas cases, however, there was a larger discrepancy between the correlations using the simulation edge conditions and the Taylor-Maccoll edge conditions. Additionally for the real gas cases, both correlations were not as true to the c_f and St extracted directly from DNS. This may be attributed to the fact that real gas effects create a thinner boundary layer, and thus the correlations may not represent the physical nature of the real gas boundary layer as accurately. It may be possible to modify the empirical parameters of the correlations used here to better suit real gas boundary layers, however such a task is outside the scope of this work.

Lastly, it was determined that the aerodynamic heat transfer rate, $\dot{Q}$, is the more critical design parameter in the hypersonic regime. The skin drag force was found to be not as sensitive to free stream conditions and wall temperature. Furthermore, the magnitude of drag attributed to skin friction was quite small and the drag savings in the laminar regime is only marginal. However, there is a substantial reduction in the magnitude of heat transfer in the laminar regime. Furthermore, the heat transfer rate was much more susceptible to changes in free stream parameters and wall temperature. Therefore, it is clear that $\dot{Q}$ is the driving factor in the design of hypersonic vehicles when considering the laminar-turbulent transition location.

In conclusion, this relatively simple analysis has shown the importance of accurately predicting or even delaying boundary layer transition to turbulence in hypersonic flows, in particular flow with high stagnation enthalpy. Turbulent flow has significantly higher skin drag and aerodynamic heating than laminar flow. Therefore, the transition location is a critical parameter in the design of hypersonic vehicles. Higher Mach number flow is shown to have higher heating than at lower Mach numbers. Additionally, the wall temperature has only a small impact on skin drag, however it can more significantly affect surface heating. Transition prediction is a complicated process and is specific to each particular flow configuration, and therefore requires in-depth and unique investigation for each particular application.

Acknowledgments

This research was supported by the U.S. Air Force Office of Scientific Research (AFOSR) through the National Defense Science & Engineering Graduate Fellowship (NDSEG) Program. This research was also partially supported by the AFOSR, USAF, under AFOSR Grant #FA9550-15-1-0268, monitored by Dr. Ivett Leyva, and by Office of Naval Research (ONR) Grant #N00014-17-1-2343, currently monitored by Dr. Eric Marineau and previously by Dr. Knox Millsaps. Primary computational resources were provided by the AFOSR with additional computational resources provided by Extreme Science and Engineering Discovery Environment (XSEDE) through Texas Advanced Computing Center (TACC) and San Diego Supercomputer Center (SDSC) under grant number TG-ASC090076, supported in part by the National Science Foundation. The views and conclusions contained herein are those of the authors and should not be interpreted as necessarily representing the official policies or endorsements, either expressed or implied, of the U.S. Air Force Office of Scientific Research, Office of Naval Research, or the U.S. Government.

References

[1]Dorrance, W. H., *Viscous Hypersonic Flow: theory of reacting and hypersonic boundary layers*, Dover Publications, Inc., Mineola, New York, 2017.

[2]Mack, L., "Computation of the Stability of the Laminar Compressible Boundary Layer," in Alder, B., Fernbach, S., and Rotenberg, M., eds., "Methods in Computational Physics," Academic Press, Vol. 4, pp. 247–299, 1965.

[3]Zhong, X. and Wang, X., "Direct Numerical Simulation on the Receptivity, Instability, and Transition of Hypersonic Boundary Layers," *Annual Review of Fluid Mechanics*, Vol. 44, 2012, pp. 527–561.

[4]Fedorov, A., "Transition and Stability of High-Speed Boundary Layers," *Annual Review of Fluid Mechanics*, Vol. 43, 2011, pp. 79–95.

[5]Leyva, I., Private Communication, 2018.

[6]Van Driest, E., "The Problem of Aerodynamics Heating," *Aeronautical Engineering Review*, Vol. 15, 1956, pp. 26–41.

[7]Goyne, C., Stalker, R., and Paull, A., "Skin-Friction Meansurements in High- Enthaply Hypersonic Boundary Layers," *Journal of Fluid Mechanics*, Vol. 485, 2003, pp. 1–32.

[8]Bres, G., Inkman, M., Colonius, T., and Fedorov, A., "Second-mode attenuation and cancellation by porous coatings in a high-speed boundary layer," *Journal of Fluid Mechanics*, Vol. 726, 2013, pp. 312–337.

[9]Fedorov, A., Soudakov, V., and Leyva, I., "Stability analysis of high-speed boundary-layer flow with gas injection," *7th AIAA Theoretical Fluid Mechanics Conference*, , No. AIAA 2014-2498.

[10]Duan, L., Wang, X., and Zhong, X., "A high-order cut-cell method for numerical simulation of hypersonic boundary-layer instability with surface roughness," *Journal of Computational Physics*, Vol. 229, No. 19, 2010, pp. 7207–7237, doi:10.1016/j.jcp.2010.06.008.

[11]Fong, K. D., Wang, X., Huang, Y., Zhong, X., McKiernan, G. R., Fisher, R. A., and Schneider, S. P., "Second Mode Suppression in Hypersonic Boundary Layer by Roughness: Design and Experiments," *Aiaa J.*, Vol. 53, No. 10, 2015, pp. 1–6, doi:10.2514/1.J054100.

[12]Haley, C. and Zhong, X., "Direct Numerical Simulation of Hypersonic Flow over a Blunt Cone with Axisymmetric Isolated Roughness," *AIAA 2017-4514*.

[13]Fong, K. D., *A Numerical Study of 2-D Surface Roughness Effects on the Growth of Wave Modes in Hypersonic Boundary Layers*, Ph.D. thesis, University of California Los Angeles, 2017.

[14]Mortensen, C. H. and Zhong, X., "High-Order Shock-Fitting Method for Hypersonic Flow with Graphite Ablation and Boundary Layer Stability," *AIAA 2012-3150*.

[15]Mortensen, C. H. and Zhong, X., "Numerical Simulation of Graphite Ablation Induced Outgassing Effects on Hypersonic Boundary Layer Receptivity over a Cone Frustum," *AIAA 2013-0522*.

[16]Mortensen, C. H. and Zhong, X., "Real Gas and Surface Ablation Effects on Hypersonic Boundary Layer Instability over a Blunt Cone," *AIAA 2013-2981*.

[17]Mortensen, C. H. and Zhong, X., "Simulation of Second-Mode Instability in a Real-Gas Hypersonic Flow with Graphite Ablation," *AIAA Journal*, Vol. 52, No. 8, 2014, pp. 1632–1652.

[18]Mortensen, C. H. and Zhong, X., "Numerical Simulation of Hypersonic Boundary-Layer Instability in a Real Gas with Two-Dimensional Surface Roughness," *AIAA 2015-3077*.

[19]Mortensen, C. H., *Effects of Thermochemical Nonequilibrium on Hypersonic Boundary-Layer Instability in the Presence of Surface Ablation and Isolated Two-Dimensional Roughness*, Ph.D. thesis, University of California Los Angeles, 2015.

[20]Knisely, C. and Zhong, X., "An Investigation of Sound Radiation by Supersonic Unstable Modes in Hypersonic Boundary Layers," *AIAA 2017-4516*.

[21]Knisely, C. and Zhong, X., "Supersonic Modes in Hot-Wall Hypersonic Boundary Layers with Thermochemical Nonequilibrium Effects," *AIAA 2018-2085*.

[22]Zhong, X., "High-Order Finite-Difference Schemes for Numerical Simulation of Hypersonic Boundary-Layer Transition," *Journal of Computational Physics*, Vol. 144, No. 2, 1998, pp. 662–709.

[23]Taylor, G. and Maccoll, J., "The Air Pressure on a Cone Moving at High Speeds. I," *Proceedings of the Royal Society of London. Series A, Containing Papers of a Mathematical and Physical Character*, Vol. 139, No. 838, 1933, pp. 278–297.

[24]MATLAB, *version 9.1.0.441655 (R2016b)*, The MathWorks Inc., Natick, Massachusetts, 2016.

[25]Bartlett, R., "Tables of Supersonic Symmetrical Flow around Right Circular Cones, with and without the Addition of Heat at the Wave," Tech. Rep. R and M No 3521, Ministry of Technology Aeronautical Research Council, 1968.

[26]Staff, A. R., "Report 1135 Equations, Tables, and Charts for Compressible Flow," Tech. rep., NACA Ames Aeronautical Laboratory, Moffett Field, CA, 1953.

[27]Eckert, E., "Engineering Relation for Friction and Heat Transfer to Surfaces in High Velocity Flow," *Journal of the Aeronautical Sciences*, Vol. 22, 1955, pp. 585–587.

[28]Crabtree, L., Dommett, R., and Woodley, J., "Estimation of Heat Transfer to Flat Plates, Cones, and Blunt Bodies," AERONAUTICAL RESEARCH COUNCIL REPORTS AND MEMORANDA 3637, R.A.E. Farnborough, 1965.

[29]Knisely, C. and Zhong, X., "The Supersonic Mode and the Role of Wall Temperature in Hypersonic Boundary Layers with Thermochemical Nonequilibrium Effects," *AIAA Paper 2018-3218*.

[30]Casper, K. M., Beresh, S. J., Henfling, J. F., Spillers, R. W., Pruett, B. O. M., and Schneider, S. P., "Hypersonic Wind-Tunnel Measurements of Boundary-Layer Transition on a Slender Cone," *AIAA Journal*, Vol. 54, No. 4, 2016, pp. 1250–1263.

[31]Holden, M., "The LENS Facilities and Experimental Studies to Evaluate the Modeling of Boundary Layer Transition, Shock/ Boundary Layer Interaction, Real Gas, Radiation and Plasma Phenomena in Contemporary CFD Codes," Tech. Rep. RTO-EN-AVT-186, NATO STO, 2010.